

AN ABSTRACT OF THE THESIS OF

Valerie J. Marty for the degree of Master of Science in Chemistry presented on October 14, 1994.

Title: Scanning Tunneling Microscopy of Organic Monolayers at the Fluid-Solid Interface

Redacted for Privacy

Abstract approved:

\_\_\_\_\_  
Philip H. Watson

More than just magnificent views of atoms and molecules, Scanning Tunneling Microscopy, STM, images have the potential to answer some fundamental questions relating to surface molecular dynamics and bonding characteristics of localized species versus more common analytical tools that provide average of bulk sample information. A special feature of the STM is utilized in this study which is the ability to image organic monolayers at liquid-solid interface at ambient conditions.

For STM analysis of organic fluids, the choice of a substrate is critical to the success of the images. The substrate must meet three criteria, the ability to sustain a tunneling current, retain an atomically flat surface over the area scanned, and immobilize a monolayer of the sample.

The adsorption geometry created by the liquid crystalline materials analyzed in this study provided magnificent detailed features of the sample monolayer on a graphite substrate. These data provide information about the balance of intermolecular forces at the interface. It is illustrated that the quality or amount of information available from any fluid-solid interfacial image is dependent upon the existence of molecular symmetry within the monolayer of the substrate surface.

Scanning Tunneling Microscopy  
of Organic Monolayers  
at the Fluid-Solid Interface

by

Valerie J. Marty

A THESIS

submitted to

Oregon State University

in partial fulfillment of  
the requirements for the  
degree of

Master of Science

Completed October 14, 1994

Commencement June 1995

APPROVED:

Redacted for Privacy

Associate Professor of Chemistry in charge of major

Redacted for Privacy

Chairman of department of Chemistry

Redacted for Privacy

Dean of Graduate School

Date thesis is presented October 14, 1994

Typed by author for Valerie J. Marty

## TABLE OF CONTENTS

	<u>Page</u>
INTRODUCTION	1
FUNDAMENTALS OF A SCANNING TUNNELING MICROSCOPE	3
A REVOLUTIONARY MICROSCOPE	3
INSTRUMENTATION	5
THEORY	12
SUBSTRATES	17
CHOICE OF A SUBSTRATE	17
GRAPHITE	18
TITANIUM OXIDE	24
GOLD ON MICA	27
ALKYL-CYANOBIIPHENYL LIQUID CRYSTAL SERIES	32
REVIEW OF LIQUID CRYSTALS	32
HEXYL-CYANOBIIPHENYL	37
OCTYL-CYANOBIIPHENYL	44
DECYL-CYANOBIIPHENYL WITH SOLVENT STUDY RESULTS	52
ALKANES AND CARBOXYLIC ACIDS	61
SUMMARY	64
REFERENCES	66

## LIST OF FIGURES

<u>Figure</u>	<u>Page</u>
1. Schematic diagram of a piezoelectric driver for the STM tip.	6
2. Illustration of a sample surface and the STM tip.	6
3. Illustration of STM operational modes. Either constant current or constant height mode can be used to produce an image by scanning in both x and y directions.	8
4. Schematic diagram of the STM instrumentation utilized in this study.	10
5. Block diagram for the feedback control system of an STM.	11
6. One-dimensional rectangular vacuum barrier of width, $d$ , between two metal electrodes with Fermi energy $E_A$ .	13
7. (a) Bias voltages within the range $V$ , allow successful electron tunneling. (b) Too large of a negative bias is unsuccessful since there are no available states to tunnel into. (c) A positive bias is unsuccessful since there are no electrons to tunnel.	14
8. Crystal structure of graphite. (a) A 3-D view. (b) The top view of the basal plane.	19
9. (a) Schematic view of the $TiO_2$ (001) surface. (b) The unit cell of rutile.	25
10. Vacuum evaporator assembly for gold deposition on mica.	29
11. Molecular structure of alkyl-cyanobiphenyl	32
12. Four basic phase transitions of thermotropic liquid crystalline materials.	33

13.	Three examples of thermotropic liquid crystal phases. The double arrow indicates the pitch to the chiral liquid crystal.	35
14.	Illustration of STM tip pierced through the liquid droplet, able to image the surface monolayer.	39
15.	Profile of 6CB monolayer on graphite, refer to Photo 10.	41
16.	Proposed structure of the 6CB liquid crystal monolayer.	43
17.	Profile of 8CB monolayer on graphite, refer to Photo 11.	45
18.	Profile of 8CB monolayer on graphite, refer to Photo 12.	46
19.	Proposed structure of the 8CB liquid crystal monolayer.	48
20.	Overlay of 8CB and 6CB molecules on graphite.	51
21.	Illustration of machined aluminum cups used to maintain graphite substrate immersed in 10CB sample-solvent solution.	55
22.	Proposed monolayer structure for 10CB adsorbed on graphite. See Table 2 for the appropriate dimensions.	58
23.	Overlay of 10CB molecules on graphite. (a) Neat sample, no solvent. (b) Decane molecules interact with alkyl chain, does not affect surface adsorption sites. (c) Dodecane molecules force the liquid crystal molecules apart.	60

## LIST OF TABLES

<u>Table</u>		<u>Page</u>
1.	Values for dimensions corresponding to Figure 16.	49
2.	Values for dimensions corresponding to Figure 22.	59

## TABLE OF PHOTOS

<u>Photo</u>	<u>Page</u>
1. STM image of HOPG basal plane. 50x50 Å, $V_b = 30$ mV, $I_t = 1$ nA.	21
2. 3-D image of graphite basal plane. 12x12 Å, $V_b = 30$ mV, $I_t = 1$ nA.	21
3. Ridge defect on basal plane of graphite. 970 x 990 Å, $V_b = 40$ mV, $I_t = 1.0$ nA.	22
4. Large area view of graphite. 450 x 450 Å, $V_b = 12$ mV, $I_t = 0.6$ nA.	23
5. Same area as illustrated in photo 4 after 7.5 V shock to upper left corner. 450 x 450 Å, $V_b = 12$ mV, $I_t = 0.6$ nA.	23
6. Titanium oxide (001) surface. 0.23 x 0.23 um, $V_b = -2.8$ V, $I_t = 0.9$ nA.	27
7. Gold film on mica. 750 x 750 Å, $V_b = 50$ mV, $I_t = 1.0$ nA.	30
8. 6CB monolayer on graphite. 750 x 750 Å, $V_b = -1.0$ V, $I_t = 1.0$ nA.	40
9. 6CB monolayer on graphite. 225 x 225 Å, $V_b = -1.35$ V, $I_t = 1.3$ nA.	40
10. 6CB monolayer on graphite with profile. 750 x 750 Å, $V_b = -1.0$ V, $I_t = 1.0$ nA.	41
11. 8CB monolayer on graphite with profile. 450 x 450 Å, $V_b = 0.77$ V, $I_t = 1.0$ nA.	45
12. 8CB monolayer on graphite with profile. 200 x 200 Å, $V_b = -0.6$ V, $I_t = 1.0$ nA.	46
13. 8CB on titanium oxide surface. 0.16 x 0.17 um, $V_b = -3.5$ V, $I_t = 0.75$ nA.	52
14. Neat 10CB on graphite 750 x 750 Å, $V_b = 1.5$ V, $I_t = 0.88$ nA.	55

15. 10CB on graphite from a decane solution. 56  
550 x 500 Å,  $V_b = -2.0$  mV,  $I_t = 1.0$  nA.
16. 10CB on graphite from a dodecane solution. 56  
410 x 400 Å,  $V_b = -1.0$  mV,  $I_t = 0.9$  nA.
17.  $C_{32}H_{66}$  on graphite from a decane solution. 62  
450 x 450 Å,  $V_b = 1.0$  V,  $I_t = 1.5$  nA.
18.  $C_{32}H_{66}$  on graphite from a dodecane solution. 62  
110 x 110 Å,  $V_b = 0.6$  mV,  $I_t = 0.8$  nA.
19. Tricontanoic acid on graphite from a decane solution. 63  
450 x 450 Å,  $V_b = 0.4$  V,  $I_t = 2.0$  nA.

# SCANNING TUNNELING MICROSCOPY OF ORGANIC MONOLAYERS AT THE FLUID-SOLID INTERFACE

## INTRODUCTION

In general level chemistry texts and courses, students are introduced to models, diagrams and illustrations to help them imagine how atoms form molecules. Sophisticated modeling programs are designed to help scientists visualize molecular structures in order to understand complex reaction mechanisms. These examples demonstrate the importance in 'seeing' what atoms and molecules look like and how it is paramount to the ability to fully understand chemical systems.

Though many tools are available that provide a variety of structural and chemical information which may lead to models and illustrations, microscopes are the tools that provide the direct visual information for localized sample characterization. The scanning tunneling microscope, STM, is a microscope which has the capability to image surface features at the atomic scale. More than just magnificent views of atoms and molecules, STM images have the potential to answer some fundamental questions relating to surface molecular dynamics and bonding characteristics of localized

species versus more common analytical tools that provide average or bulk sample information.

A special feature of the STM, which is utilized in this study, is the ability to image organic monolayers at the liquid-solid interface at ambient conditions. Since this is a new technology, the experimentation and development which must be carried out to determine the full capabilities of the scanning tunneling microscope is just beginning. Problems which need to be addressed include how to develop a sample preparation methodology, what parameters contribute to successful images and whether the interpretation of the data is accurate.

## FUNDAMENTALS OF A SCANNING TUNNELING MICROSCOPE

### A REVOLUTIONARY MICROSCOPE

**Microscope** "An optical instrument that uses a combination of lenses to produce magnified images of small objects, especially of objects too small to be seen by the unaided eye."<sup>1</sup>

The American Heritage Dictionary of  
the English Language

Before the 1980's, microscopy was made possible by the use of optical lenses. The resolution of light microscopes is theoretically limited by the wavelength of the imaging light, to features on the order of two hundred nanometers (nm). In the 1930's, Ernest Ruska developed the electron microscope, which incorporated high energy electrons as the primary source.<sup>2,3</sup> The theoretical resolving power for wavelengths associated with electron beams alone indicate that  $10^{-3}$  nm resolution could be possible, though the final limits on what may be observed are due to non ideal optics and the damaging effects of the illuminating beam. After years of improving the quality of lenses and the electron guns used, the technology of electron microscopy has met with resolution limitations on the order of a nanometer for biological samples and 0.1 nanometer for materials-science applications.<sup>3</sup>

During the last decade, the traditional definition of microscopy was altered by Heinrich Rohrer and Gerd Binnig, principle inventors of the scanning tunneling microscope, STM.<sup>4,5</sup> In 1978, at the IBM Research Division in Zurich Switzerland, their research focused on developing a tool for local spectroscopy using principles of quantum mechanical tunneling.<sup>6</sup> During their work, the concept to incorporate piezoelectric materials as a driver mechanism was utilized. While attempting tunneling spectroscopy, the researchers made modifications making it possible to obtain topographic information from a surface. Further efforts resulted in the first scanning tunneling microscope. As a microscope which no longer requires traditional optics, the STM design features a piezoelectric driver mechanism, electronic feedback circuitry and data imaging software. With the introduction of a microscopic technology based on the principles of quantum mechanical tunneling, the possibility for higher resolution were no longer limited to the wavelength of a photon source.

By 1982, STM technology began gaining recognition. Binnig and Rohrer et. al. published the first STM image of silicon, a semiconductor surface, in 1983.<sup>7</sup> Atomic resolution of the Si(111) surface proved to be an exciting example which provided additional evidence for the accepted

(7 x 7) reconstruction pattern of the silicon surface. <sup>7,8</sup> Later that year, Au(111)-(1x2), another well-studied surface, was imaged by the same investigators<sup>9</sup>, again confirming the previously proposed structure. In 1986, Binnig and Rohrer shared the Nobel Prize in Physics with Ernest Ruska. The definition of the term microscope must now be changed to include the technological advancements introduced by the STM.

"Microscopes, in the most general sense, must be redefined as instruments that directly provide maps of specimen detail at resolutions superior to those obtainable by direct observation."<sup>3</sup>

Elizabeth Slayter and Henry Slayter  
Light and Electron Microscopy

## **INSTRUMENTATION**

The imaging probe of an STM is a conductive metal tip, attached to a piezoelectric crystal. Piezo ceramic materials have the unique ability to expand and contract in a minute and precise motion when an electric field is applied across the crystal's plane of polarization. Usually manufactured in a tubular design for use in STMs, the crystal has a conductive silver coating separated into four sections illustrated in Figure 1. The piezo driver must be carefully calibrated to allow the appropriate voltages which are supplied to each quadrant. The tip is therefore able to

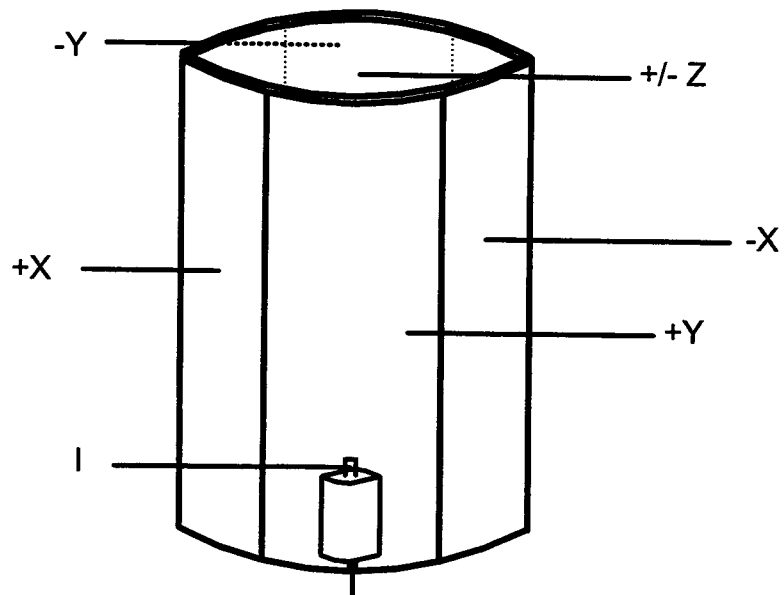


Figure 1. Schematic diagram of a piezoelectric driver for the STM tip.

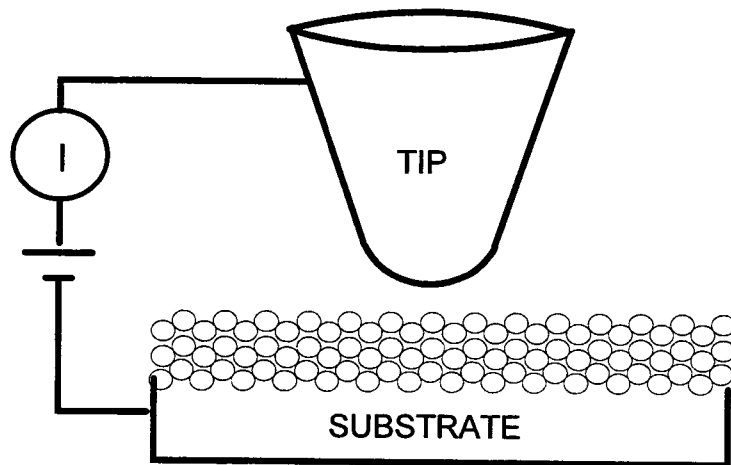


Figure 2. Illustration of a sample surface and the STM tip.

scan across a substrate surface along a horizontal plane. A uniform silver coating upon the interior surface of the tube, allows for lateral placement control of the tip.

The tip is brought extremely close to the sample surface, with separation distances typically on the order of one nanometer. An applied bias potential is created between the tip and sample, Figure 2, allowing a small tunneling current to flow. Standard operating parameters incorporate bias voltages on the order of a volt and tunneling currents close to a nanoamp. During data acquisition, the piezoelectric crystal drives the tip parallel to the plane of the sample surface, while the tunneling current and piezoelectric circuitry are constantly monitored.

For simplicity, imaging modes can be classified in two categories, constant height and constant current, Figure 3. In constant height mode, after the tip is brought sufficiently close to the surface in order to establish a tunneling current, no further vertical displacement of the tip is made. Variation in the tunneling current is monitored as the piezo scans across a two-dimensional plane. Constant current mode is opposite, in that the voltage applied to the vertical displacement section of the piezo is the primary signal monitored during a scan while a feedback

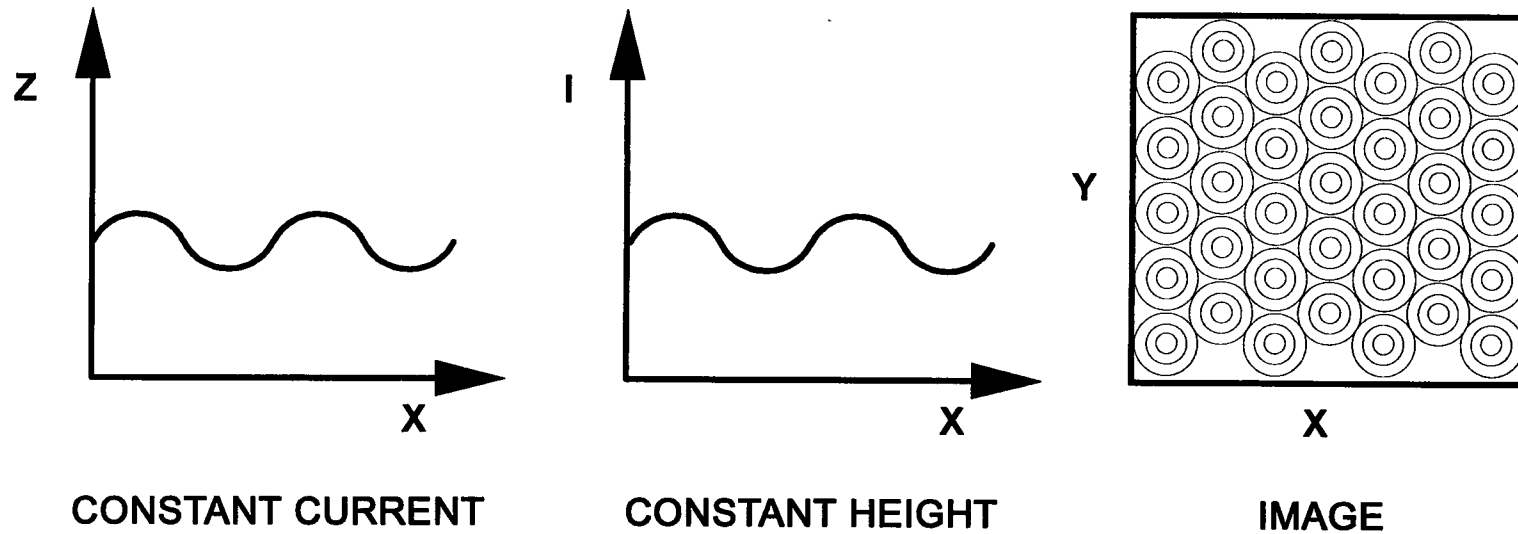


Figure 3. Illustration of STM operational modes. Either constant current or constant height mode can be used to produce an image by scanning in both x and y directions.

loop maintains the tunneling current at a constant preset value. The primary advantage of the constant height mode, is the advanced speed obtained without a feedback loop in the circuitry. The disadvantage of constant height mode is the greater probability of damaging the tip by crashing into large surface features. In either case an analog to digital conversion enables the signal to be displayed as an image on a video screen.

The STM which was used for the analysis presented in this study is depicted in Figure 4. The STM body and control electronics were purchased from Digital Instruments Inc. and packaged as the Nanoscope I Scanning Tunneling Microscope. It utilizes a pseudo constant height mode which incorporates a feedback loop as a safety feature to reduce the chance of a tip "crashing" into the surface, Figure 5.<sup>10</sup> The microscope body houses the ceramic piezoelectric driver, tip and sample mount along with a coarse positioning motor and the preamplifier. Connected to the STM body is the control electronics unit which includes further amplifiers, feedback circuitry, parameter adjustment controls and LED data readouts. The microscope body is placed on a covered cement slab, suspended from the ceiling by elastomeric cords for vibration isolation.

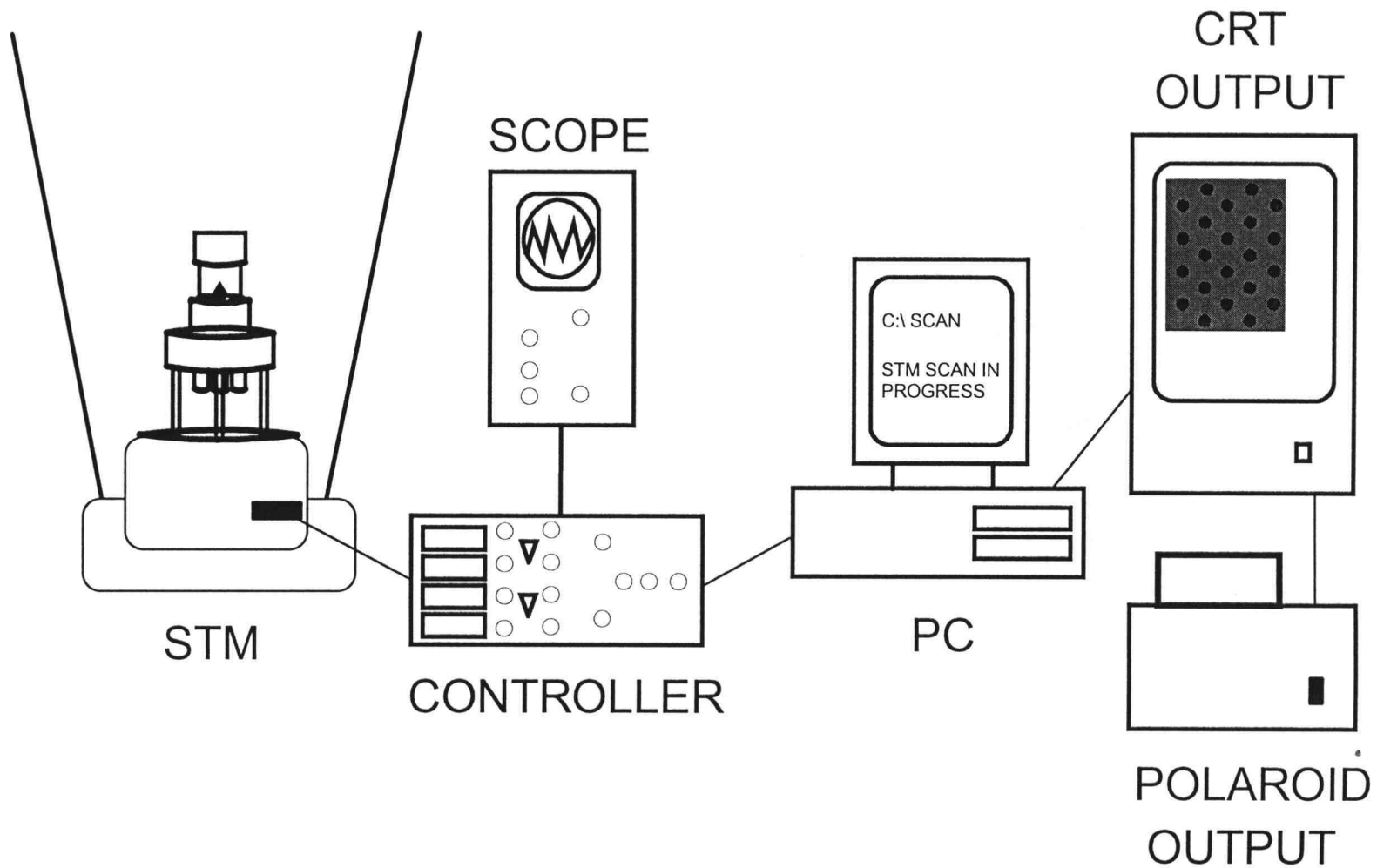


Figure 4. Schematic diagram of the STM instrumentation utilized in this study.

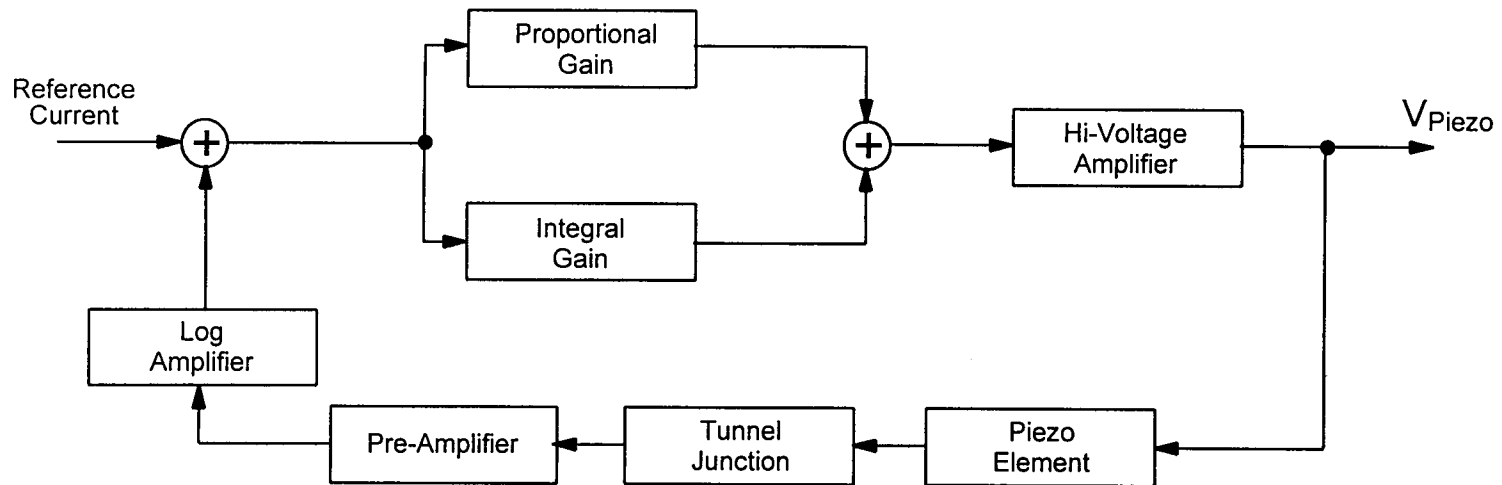


Figure 5. Block diagram for the feedback control system of an STM.

Data acquisition is obtained by use of an IBM 286 compatible computer interfaced to the Nanoscope I. The command language for a Data Translations image processing board and DT-IRIS device driver was written in Quick C by fellow graduate student Glenn Tinseth. Resulting images were saved on the hard disc, displayed on an RGB color monitor, and photographed with a Polaroid Freezeframe video image recorder.

## **THEORY**

Tunneling is a quantum mechanical process whereby an electron is able to pass through an energy barrier which is forbidden in classical physics. The one-dimensional rectangular vacuum barrier model introduces the basic principles demonstrated by an STM, Figure 6.  $E_A$  corresponds to the Fermi energy levels in equilibrium of two metal electrodes. A tunneling current is established by the electrons which are able to pass through the vacuum barrier gap.

Measured by the tunneling current  $I$ , the probability of electron transmission is sensitive to the value of  $d$ , the vacuum gap distance between electrodes,

$$I \propto e^{-2kd}. \quad (1)$$

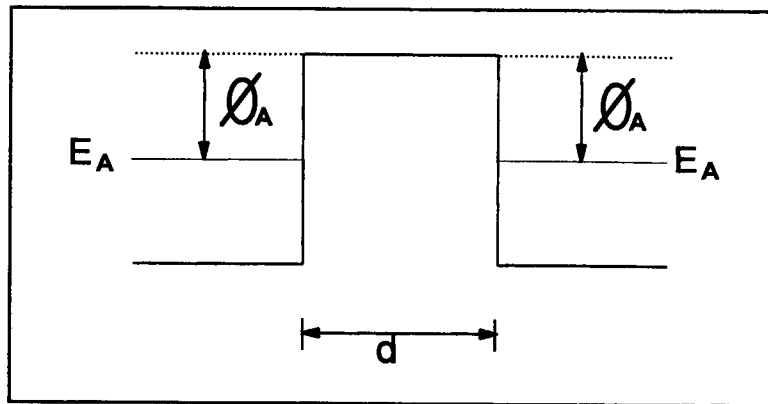


Figure 6. One-dimensional rectangular vacuum barrier of width,  $d$ , between two metal electrodes with Fermi energy  $E_A$ .

This relationship originates from the solution of the Shrodinger equation inside a one-dimensional rectangular barrier,<sup>11</sup>

$$\psi = e^{\pm Kz}. \quad (2)$$

To solve the equation, the critical parameter is the wavenumber  $\kappa$ , where

$$\kappa^2 = 2m(V_b - E)/\hbar^2. \quad (3)$$

Expanding the argument, to a trapezoidal barrier, Figure 7 illustrates three scenarios for two metal electrodes with Fermi energy levels not in equilibrium. In this model, electron tunneling occurs only when there is an allowable bias voltage  $V$ , applied. For successful tunneling, accessible energy states must be available.

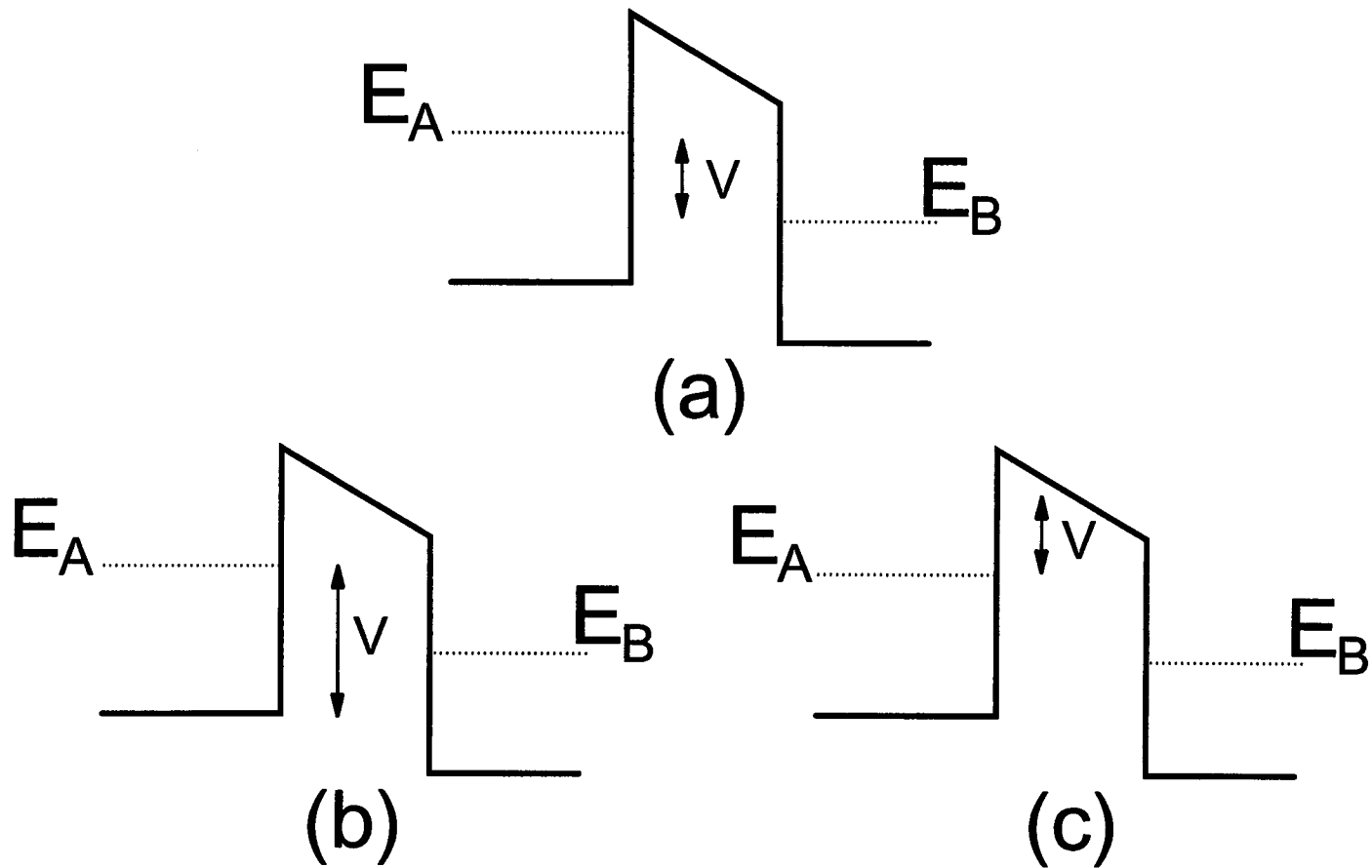


Figure 7. (a) Bias voltages within the range  $V$ , allow successful electron tunneling. (b) Too large of a negative bias is unsuccessful since there are no available states to tunnel into. (c) A positive bias is unsuccessful since there are no electrons to tunnel.

The basic principle of quantum mechanical tunneling portrayed in Figure 7 (a), corresponds well to a simplified model of the tip-sample interaction found in scanning tunneling microscopy. Since the tunneling current measured by an STM is related to the gap distance between the tip and sample, the resulting image can be thought of as a topographical representation of the sample surface. For the most part, such a simple model is adequate for interpreting STM images with resolution on the scale of a nanometer or larger. Features on the atomic scale require a more detailed approach.

Bardeen's transfer Hamiltonian approach<sup>12</sup>, utilizes perturbation theory and forms the basis of the more recent theoretical STM formalisms<sup>13, 14, 15, 16</sup>. Originally, the technique was designed to study the tunneling current flowing in MIM devices, two conducting metals separated by an insulating material. Bardeen's theory assumes that the metals are weakly coupled and a common Hamiltonian of the insulator can be used for both electrodes.<sup>17</sup> This simplified calculations and transferred the focus for calculating the tunneling current to the approximation of the metal electrode wave functions.

A close comparison can be made between the tunneling process in a traditional MIM device and the STM. An important step toward understanding STM results using Bardeen's formalism, requires an appropriate model of the tip and substrate metals. This is not a trivial problem. By modeling an "ideal" tip, in a vacuum system Tersoff and Hamann<sup>18</sup> have proposed that the tunneling current is proportional to the surface local density of states, LDOS, at the Fermi level, where the tip is positioned.

For STM images of organic monolayers, the tunneling mechanisms are even more complicated. "In some cases, it has been postulated that the molecular contrast originates from the variation in work function due to the adsorption of the molecules, while in others the electronic structure of hybridized molecule-substrate orbitals appears to be more important."<sup>19</sup> Without a clear understanding of the tunneling process for molecular adsorbates, data interpretation is made more difficult. As greater numbers of successful STM images provide incontestable results, the additional data will support more accurate theoretical mechanisms. The continuation of this process will help to determine the future of scanning tunneling microscopy.

## **SUBSTRATES**

### **CHOICE OF A SUBSTRATE**

A primary requirement for an STM image is the ability to obtain a tunneling current. This factor makes STM imaging of organic materials difficult, since many such samples are insulators. By placing a single thin organic monolayer upon a conductive substrate, it is possible for the tunneling electrons to cross the insulating barrier and maintain a current. Since the resultant image is altered by the adsorbate, compared to an image of the clean substrate surface, the image of the surface monolayer can provide information about the studied organic material.

A successful substrate must also provide an atomically flat surface which readily adsorbs the sample being studied. An atomically flat surface is needed so that structural features of the substrate are not confused with features resulting from the adsorbate material. Immobilization of the sample is necessary and obtained through surface adsorption. It becomes impossible to obtain structural information about the material when it is being dragged along by the tip as it scans across the surface. The data presented in the following sections describe some of the

strengths and weaknesses of the three various substrates that were analyzed in this study.

## **GRAPHITE**

The immediate advantage of using graphite as a substrate is the ability to obtain a clean, atomically flat surface extremely easily. Cleaving a crystal of highly oriented pyrolytic graphite, HOPG, to prepare a fresh surface is literally as simple as placing a piece of adhesive tape on the old surface and peeling it back. Figure 8 illustrates the crystal structure which helps to explain this desirable property.

The basal planes consist of carbon atoms arranged in a hexagonal geometry. Within a plane, the interatomic distance is 1.41 Å. These atoms are strongly held together by a conjugated pi bonding system. Individual planes are stacked in an alternating ABA sequence with a spacing of 3.35 Å.<sup>20</sup> Weak Van der Waals forces loosely bind the planes which allows for easy cleavage. The result is an atomically flat surface.

With a minimal resistivity of 0.04 miliohms/cm at room temperature<sup>20</sup>, a tunneling current is obtainable. A

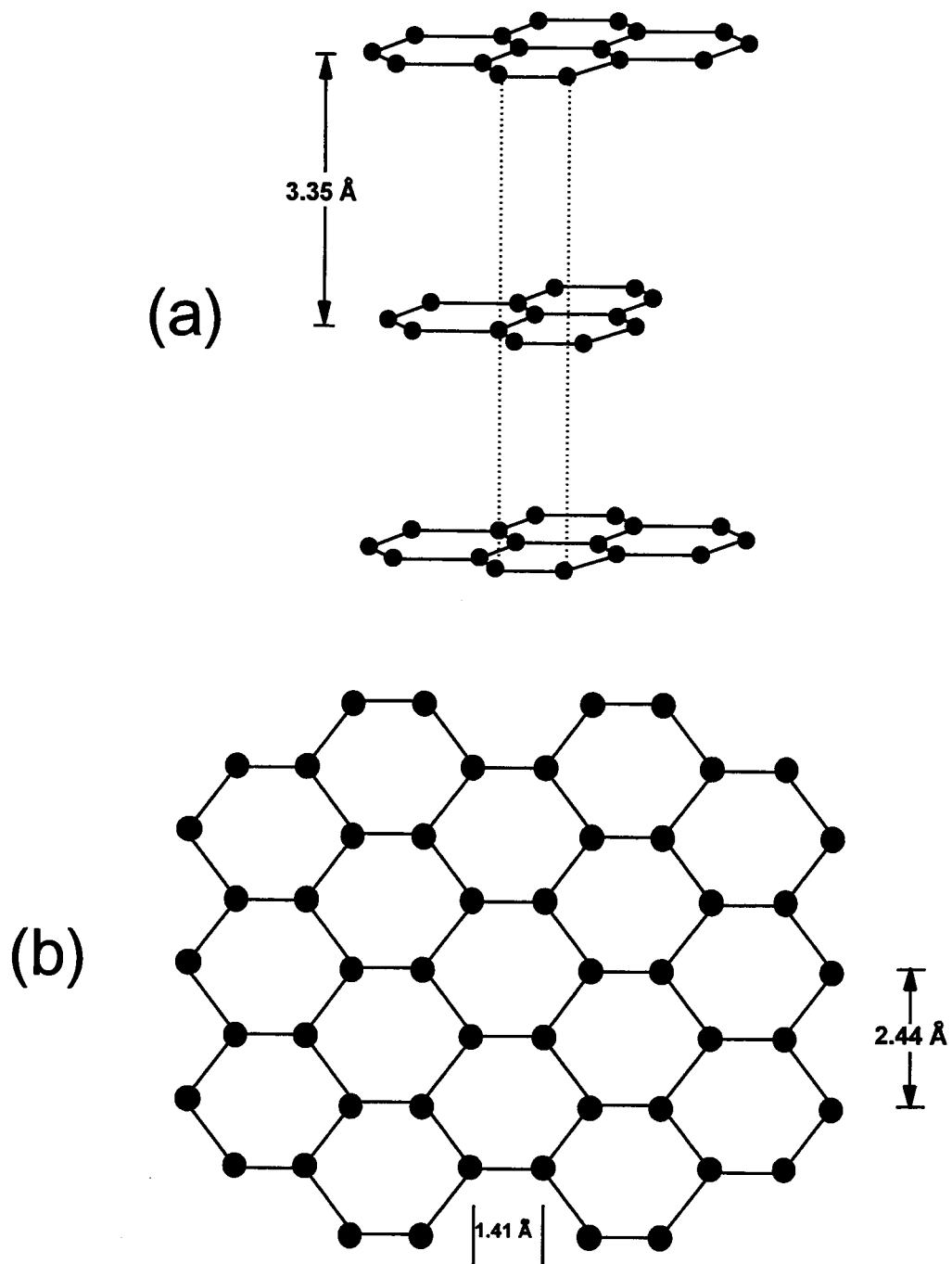


Figure 8. Crystal structure of graphite. (a) A 3-D view. (b) The top view of the basal plane.

successful STM image of an HOPG surface is presented in Photo 1. These data do not directly correspond to the expected hexagonal pattern displayed by Figure 8. Instead of the 1.41 Å interatomic spacing, the resulting calculations based on the STM image determine a lattice spacing of 2.4 Å, which agrees with the distance between alternate atoms in the crystal structure. An overlay of a graphite basal plane upon an STM image is illustrated in Photo 2. This shows how the STM appears to "see" only every other atom. With the ABA stacking pattern of the planes in graphite, only half of the carbon atoms have an atom directly below on the next plane. This creates two unique electronic environments between the two types of atoms. Only one of the two types are therefore detected by the STM.

Though HOPG is highly ordered, it is possible to observe common defects such as fibers, flakes, strands, steps and ridges on a freshly cleaved surface. When using graphite as a substrate for STM studies, it is important to be familiar with these various defects. For instance, a study by Clemmer and Beebe<sup>21</sup> has described how STM features of graphite can mimic the structure of DNA and other molecules. After scanning across various areas of the surface, it may not take long before a suitable area is found or another cleaved surface is made. Photo 3 is a

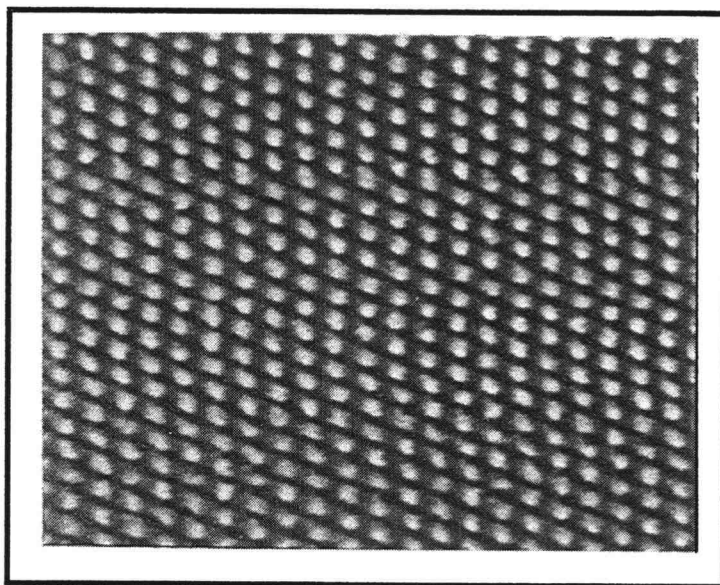


Photo 1. STM image of HOPG basal plane.  
 $50 \times 50 \text{ \AA}$ ,  $V_b = 30 \text{ mV}$ ,  $I_t = 1 \text{ nA}$ .

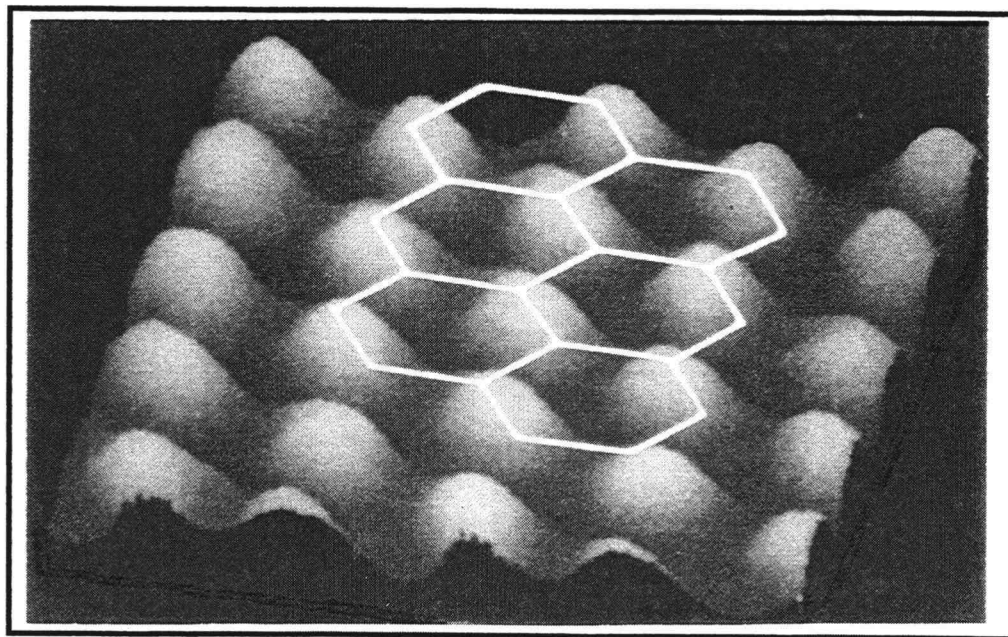


Photo 2. 3-D image of graphite basal plane.  
 $12 \times 12 \text{ \AA}$ ,  $V_b = 30 \text{ mV}$ ,  $I_t = 1 \text{ nA}$ .

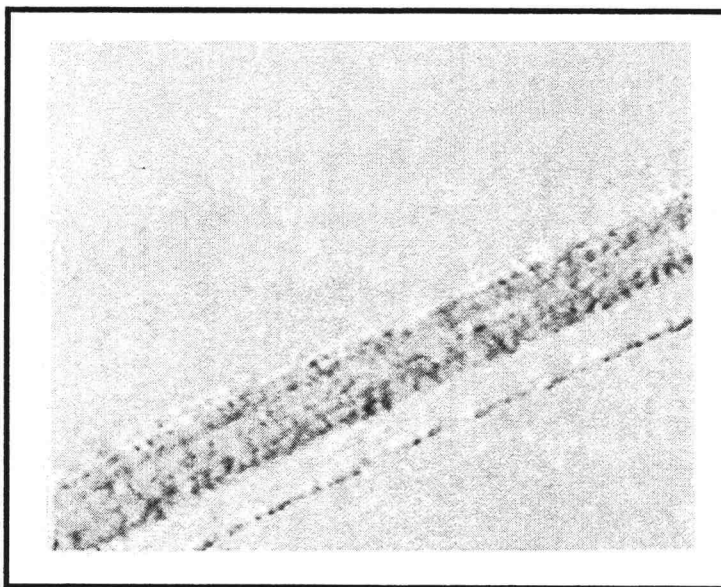


Photo 3. Ridge defect on basal plane of graphite.  
970 x 990 Å,  $V_b = 40$  mV,  $I_t = 1.0$  nA.

representative STM image of a ridge type defect. By focusing on the top left segment of the image, it was possible to obtain atomic resolution near the defect.

It is also possible to create defects while scanning. photos 4 and 5 illustrate this point. The before image shows a flat surface of graphite, lacking any features. While resting at the top-left position, the tip bias was increased to 7.5V. The after image shows the extreme destruction caused by the high energy electrons. Scanning conditions must be maintained at parameters which minimize damaging effects while providing a steady tunneling current.

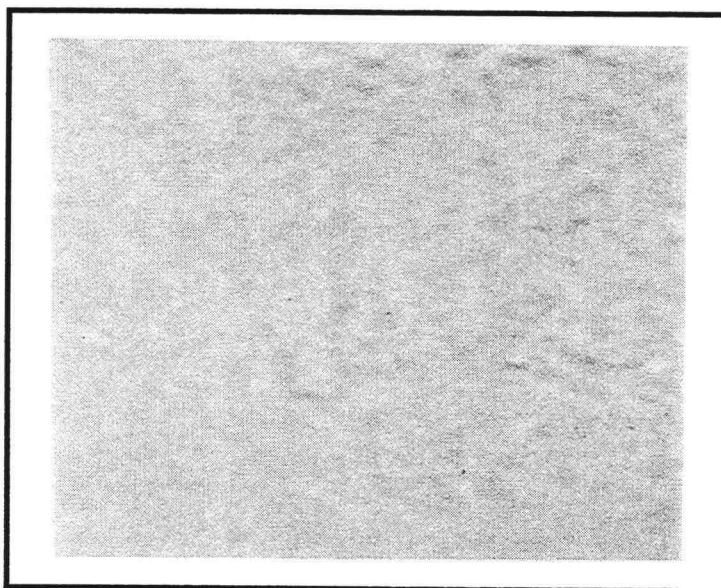


Photo 4. Large area view of graphite.  
 $450 \times 450 \text{ \AA}$ ,  $V_b = 12 \text{ mV}$ ,  $I_t = 0.6 \text{ nA}$ .

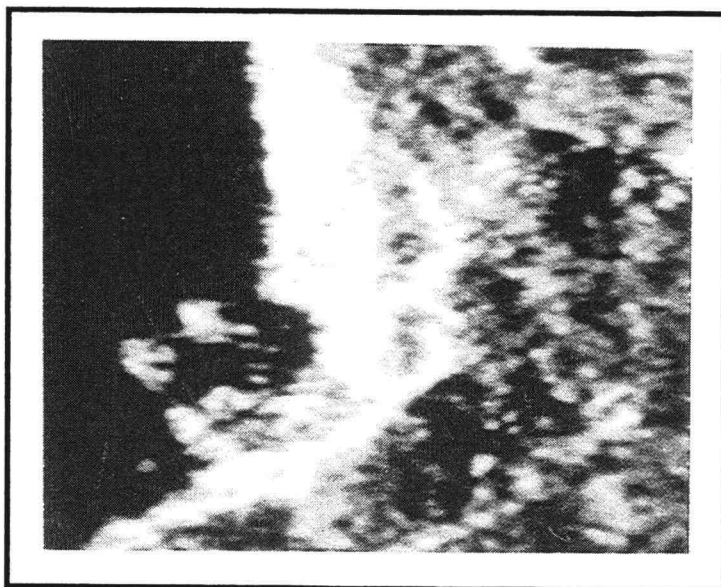


Photo 5. Same area as illustrated in photo 4 after  
7.5 V shock to upper left corner.  
 $450 \times 450 \text{ \AA}$ ,  $V_b = 12 \text{ mV}$ ,  $I_t = 0.6 \text{ nA}$ .

The ease of obtaining an atomically flat surface is desirable, but it alone does not make graphite a universally acceptable substrate for STM studies of organic monolayers. The conjugated pi system which allows for easy cleavage, also creates a very stable, non reactive surface. This property is helpful in maintaining a clean surface, but it also makes sample immobilization by chemabsorption difficult. Whether graphite can be used is therefore dependent upon the chosen sample. In an attempt to obtain alternative substrates, TiO<sub>2</sub> and gold evaporated upon mica were studied.

#### **TITANIUM OXIDE**

Unlike graphite, rutile does not have a crystal structure which facilitates easy preparation of a suitable surface.<sup>22</sup> See Figure 9. The unit cell contains one titanium atom and two oxygen atoms with a lattice constant of 4.594 Å. Successive layers within the crystal differ by a 90° rotation and diagonal offset of 3.248 Å. The titanium oxide crystal used in this study was obtained from Commercial Crystals Inc. and was cleaved along the (001) surface plane.

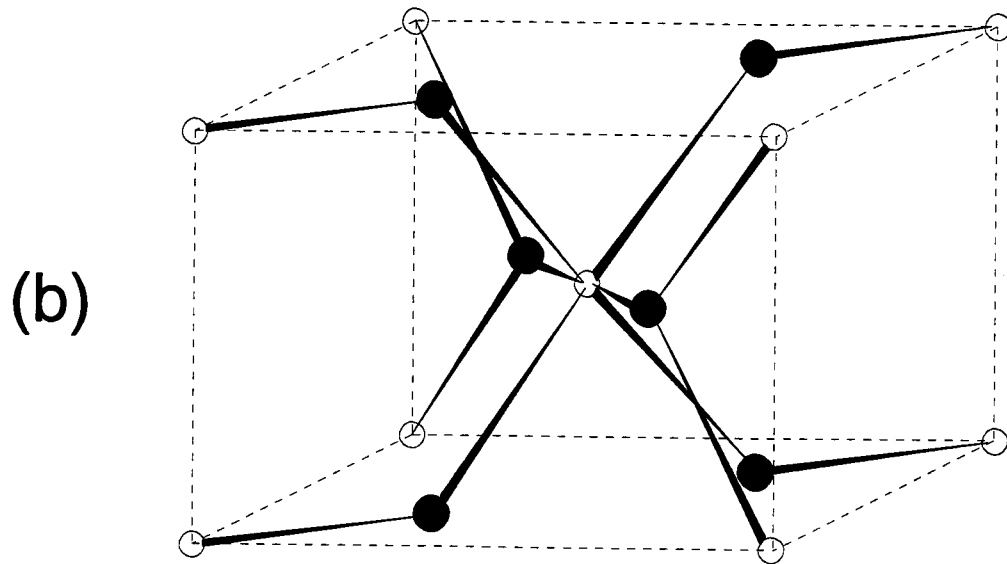
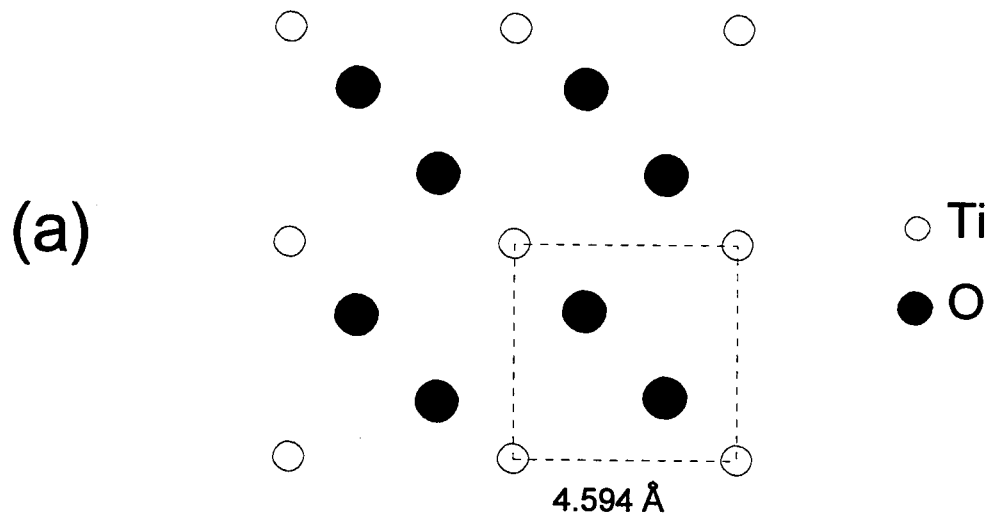


Figure 9. (a) Schematic view of the  $\text{TiO}_2$  (001) surface.  
(b) The unit cell of rutile.

To provide sufficient conductivity for STM imaging, reduction was required to obtain an n-TiO<sub>2</sub> doped crystal. Laboratory procedure employed a furnace chamber filled with a 5:1 H<sub>2</sub>/Ar gas mixture. Dual ramp and dual dwell time features controlled the heating process. The colorless, clear TiO<sub>2</sub> crystal was placed in the furnace. Ramp settings were set at 200°C/hr. After 300°C was reached, the temperature was maintained for one hour. The temperature was then increased to 800°C and held for an additional 30 minutes. The furnace was then allowed to cool at 100°C/hr. until room temperature was obtained. After cooling, the crystal appeared blue/gray indicating successful reduction. The (001) surface became hazy and required repolishing.

Carbide polishing compounds were employed to repolish the crystal surface. A 600 mesh polish was obtained with silicon carbide. A 5.0 um finish was obtained with a series of aluminum oxide polishes. Micropolishes down to grade gamma alumina in an aqueous solution of HF achieved a 0.05um polish. The crystal was then placed in a sonic bath with a solution of H<sub>3</sub>PO<sub>4</sub> for further chemical etching.

Photo 6 is a resulting STM image of the TiO<sub>2</sub> crystal. Though the successful reduction procedure created the possibility to image the surface, the resulting features



Photo 6. Titanium oxide (001) surface.  
0.23 x 0.23  $\mu\text{m}$ ,  $V_b = -2.8 \text{ V}$ ,  $I_t = 0.9 \text{ nA}$ .

produced from polishing process are more prominent than desired for as a substrate. Unless more elaborate methods were to be utilized for polishing the crystal, use of  $\text{TiO}_2$  did not appear to show great potential as a substrate. Results obtained with liquid crystals on  $\text{TiO}_2$  will be displayed in the next chapter.

#### **GOLD ON MICA**

Mica is similar to graphite in that it is easy to cleave a fresh clean surface without requiring additional polishing. Mica alone can not be used as a substrate for STM studies due to the high resistivity of the material. By

placing a thin gold film upon mica, it is possible to obtain a conductive substrate utilizing the flat surface of the mica and high conductivity of gold. As commonly used in electron microscopy, vacuum evaporation techniques can be utilized to deposit thin gold films.

In the laboratory, we used a vacuum evaporator apparatus as illustrated in Figure 10. Green muscovite mica, obtained from Ashville-Shoomaker Mica Company was placed upon a copper heating mantel within the bell jar. Gold wire was wrapped around a tungsten filament placed approximately five inches above the mica surface. A mechanical roughing pump was used to obtain low enough pressures to engage the ion pump. One variac supplied the current across the filament, another variac controlled the temperature of the copper heating mantel. The thermocouple probe was placed near the mica on the heating mantel. Once the mica reached a temperature of 500°C, current was slowly increased to the tungsten filament. After the gold melted to a round ball, the metal was allowed to evaporate slowly.

An image of a gold film is displayed in Photo 7. Over the area scanned, the surface appears to lack large structures and can be considered relatively featureless. The image appeared blurry while scanning the smaller area,

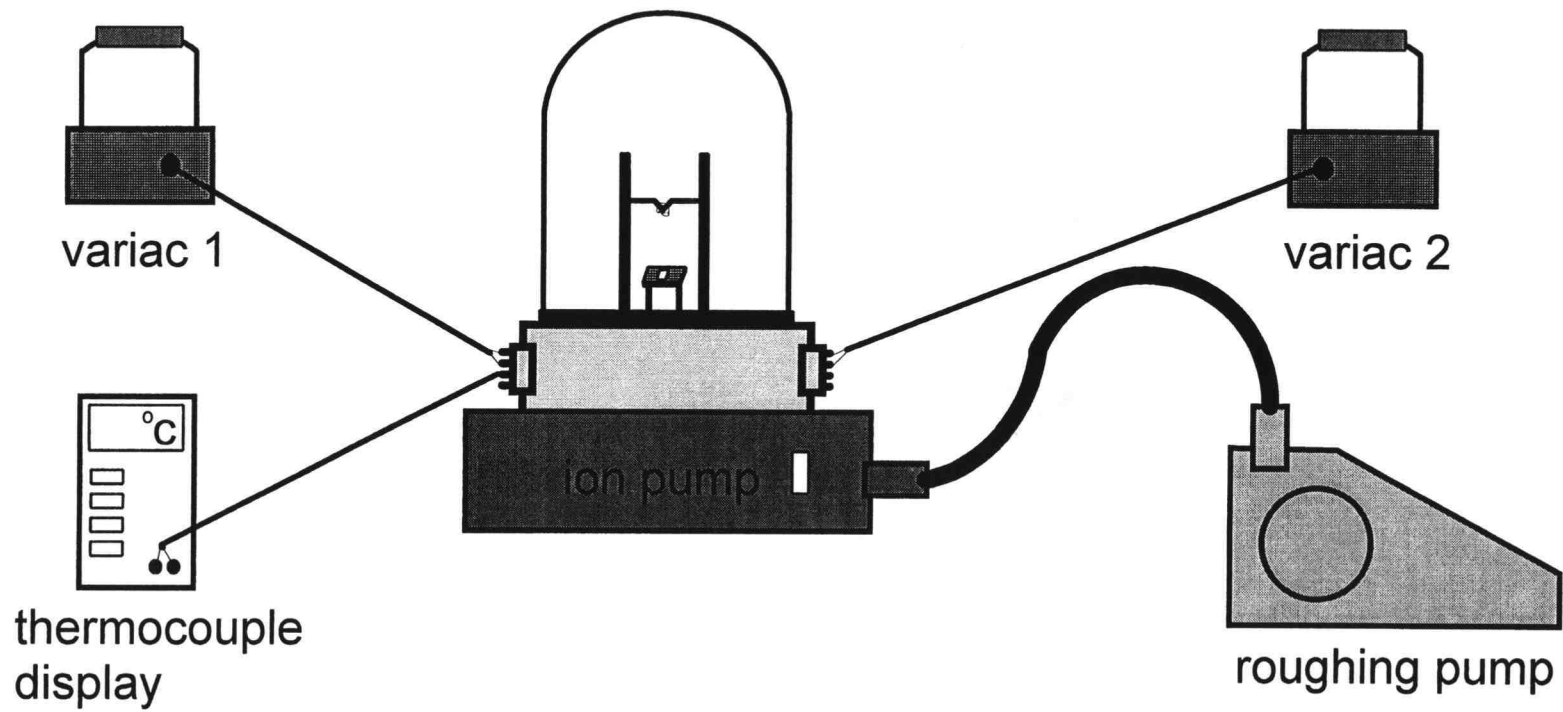


Figure 10. Vacuum evaporator assembly for gold deposition on mica.

failing to resolve atomic features. At this point, difficulties were encountered with the ion pump when preparing another film. Time constraints prohibited further study of gold on mica as a substrate for organic monolayers.

Others have reported successful STM images of the Au(111) surface of gold on mica.<sup>23,24</sup> Best results have been noted as being taken as soon as possible after the fresh gold surface is removed from vacuum. When deposition conditions are properly maintained, the surfaces tend to be atomically flat over a few micrometers, consisting of terraces at about 1000 Å wide, separated by monatomic steps

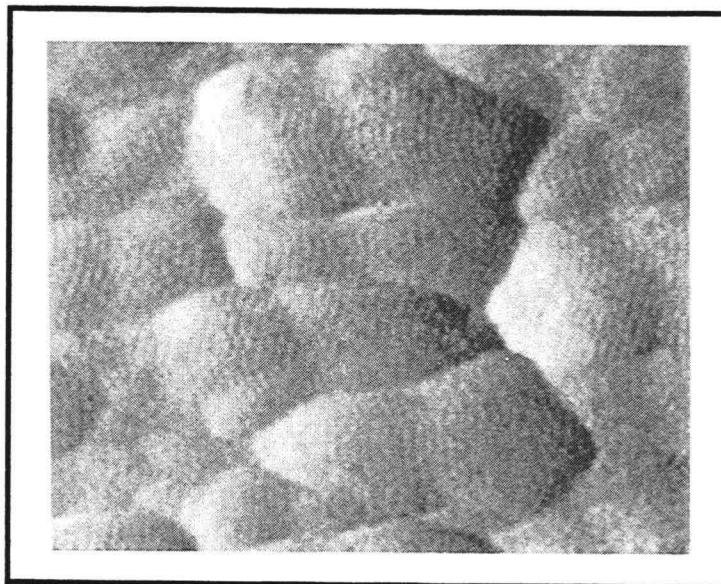


Photo 7. Gold film on mica.  
750 x 750 Å,  $V_b = 50$  mV,  $I_t = 1.0$  nA.

of 2.36 Å in height. This can be considered an good STM substrate surface, which incorporates just occasional grain boundaries.<sup>25</sup>

**ALKYL-CYANOBIPHENYL LIQUID CRYSTAL SERIES****REVIEW OF LIQUID CRYSTALS**

Alkyl-cyanobiphenyl liquid crystals adopt the generic structure represented in Figure 11, and are abbreviated as nCB, with n representing the number of carbon atoms within the alkyl chain. Octyl-cyanobiphenyl would therefore be designated 8CB.

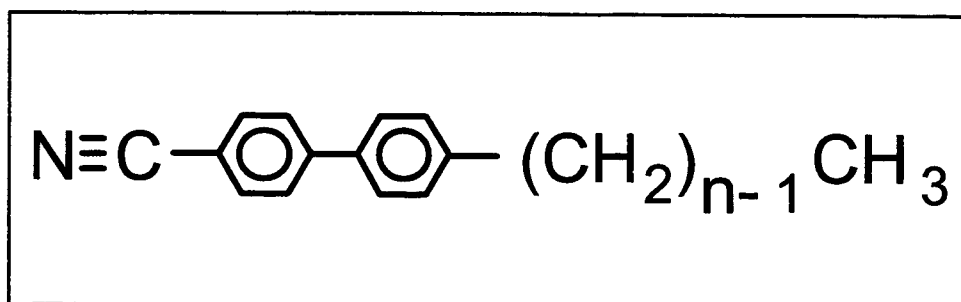


Figure 11. Molecular structure of alkyl-cyanobiphenyl.

Of the various classifications of liquid crystalline materials, the alkyl-cyanobiphenyl series used in this study, 6CB, 8CB and 10CB are thermotropic liquid crystals, which were obtained from EM Industries. The term 'liquid crystal' defines a particular phase of a compound which exhibit properties that combine those of liquids and solids. For thermotropic liquid crystals, the phase change is created by a variation in temperature, keeping other

conditions constant. The mesophase refers to the state when the material exhibits liquid crystalline properties. See Figure 12.

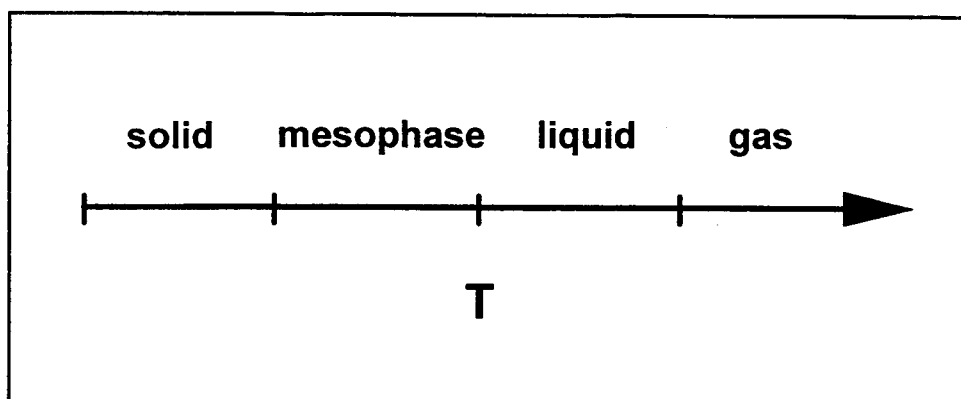


Figure 12. Four basic phase transitions of thermotropic liquid crystalline materials.

Individual molecules within a bulk solid are constrained in both crystal lattice position and the way in which they orient themselves to one another. Molecular interactions create large constraints upon individual molecular alignment, and the strength of the interactions determines the physical state of the material. Attractive intermolecular forces increase as a material changes from a gas to liquid then to a solid. When a solid melts into a liquid, both positional and orientational order are lost. When liquids vaporize to the gas phase, there is even greater positional randomness and increased intermolecular distances are obtained. Both liquids and gases have the

ability of forming to the shape of the container in which they are held.

When a solid melts to a liquid crystal, however, rigid positional order is lost, while some degree of orientational order is maintained. With no positional order, a liquid crystal also takes on the shape of its container, though the degree of fluidity for each liquid crystal is dependent upon the unique intermolecular forces present in the system. It is common for materials in their liquid crystalline phase to appear cloudy or opalescent due to refraction of light from the partial molecular orientation.

Liquid crystals are classified into unique classifications dependent upon how the molecules maintain their intermolecular orientation while in the liquid crystalline phase. Using simple linear molecules in a model, Figure 13 illustrates three liquid crystalline forms. This model is oversimplified, in that all the molecules appear to be aligned parallel with one another. Liquid crystalline molecules maintain only a preferred alignment, designated as the director, with some limited variability to rotation by some degree ( $\Theta$ ). The greater the  $\Theta$  for a given liquid crystal, the more "liquid like" the liquid crystal is. Small  $\Theta$  values indicate "solid like" properties. For

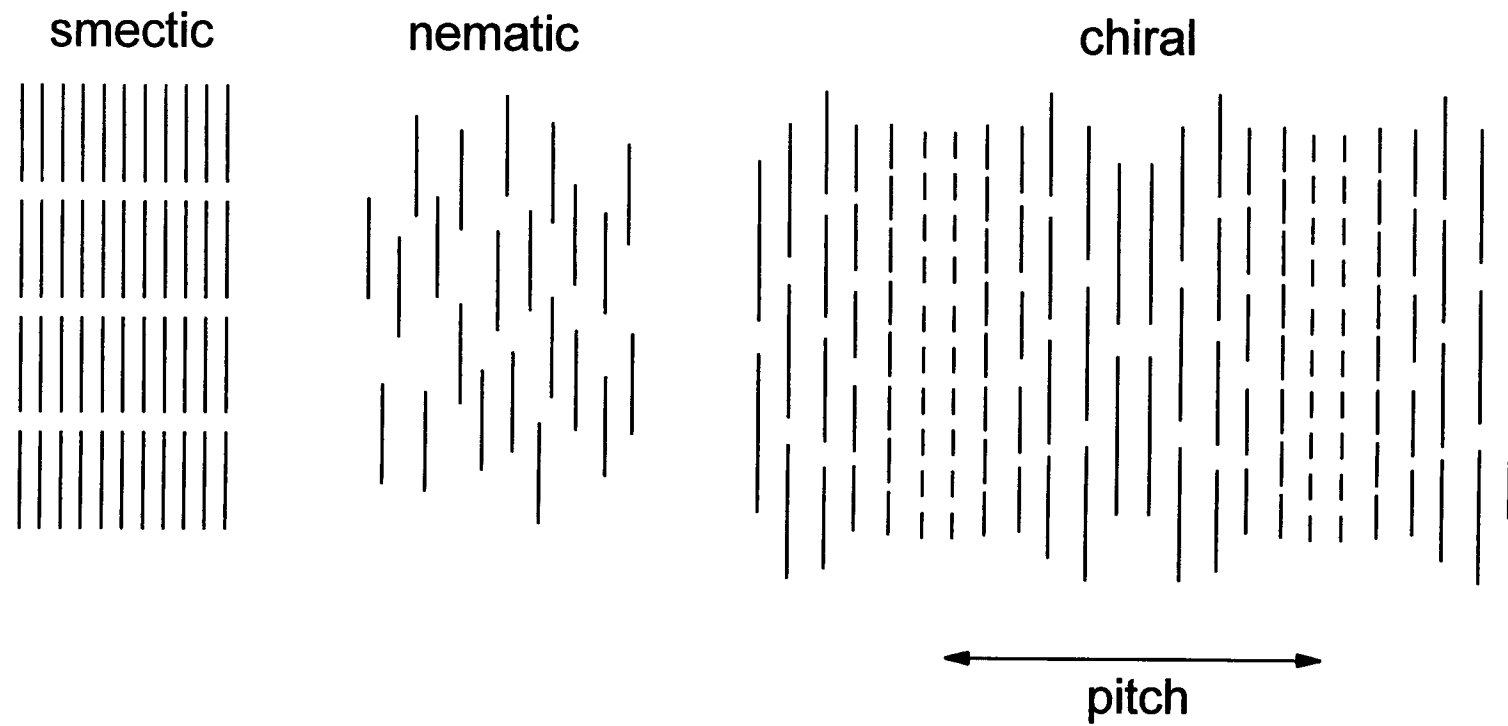


Figure 13. Three examples of thermotropic liquid crystal phases. The double arrow indicates the pitch to the chiral liquid crystal.

chiral liquid crystals, the director rotates about an axis and the pitch is defined as the length required for the director to rotate one full revolution.

The unique molecular alignment found in smectic liquid crystals provides a desirable quality for a scanning tunneling microscopy study. When attempting to image an organic monolayer, if there is no positional or orientational order, useful results are largely dependent upon resolution of individual molecules, for there would be no other structural features to resolve. Interpretation of such images can be difficult and limited. When there is molecular alignment as found with smectic liquid crystals, STM resolution of the intermolecular and molecular structures provide greater information from a successful image.

The first publication reporting scanning tunneling microscope images of organic monolayers was presented by Foster and Frommer.<sup>26</sup> Their results included an image of the liquid crystalline material octyl-cyanobiphenyl on graphite. Since then, there have been further studies featuring the alkyl-biphenyl series.<sup>27, 28, 29</sup> Approaches to preparing the samples have varied. Earlier attempts struggled to prepare very thin films of the liquid crystals. Smith et. al.<sup>28</sup>

achieved thin films by heating the sample above 100°C to sublime the liquid crystal upon the substrate. Mizutani et. al.<sup>29</sup> placed a drop of the sample upon the graphite, heated above the isotropic phase and allowed the sample to cool to the mesophase temperature range. Such extraneous techniques did not prove to be essential. Sample preparation methods are described in greater detail in the following sections.

#### **HEXYL-CYANOBIPHENYL**

Of the three liquid crystalline materials studied, hexyl-cyanobiphenyl, or 6CB, has the lowest melting point at 15°C. The clearing point, to the isotropic liquid phase, is at 29°C. The material has the appearance of a white opalescent fluid. 6CB is a nematic thermotropic liquid crystal at ambient conditions, whereas both 8CB and 10CB are smectic liquid crystals.

The procedure for sample preparation began with a freshly cleaved surface of graphite. Large areas of the graphite were then imaged to determine the availability of large featureless terraces upon the basal plane. When there was difficulty finding such areas, the graphite was cleaved again, until a high quality surface was produced. Smaller areas were then imaged to analyze whether the tip was

damaged. If atomic resolution was possible with graphite alone, the tip was acceptable for further imaging. After the tip and substrate were determined to be ready, a drop of the liquid crystal was placed upon the graphite surface.

The substrate and sample were mounted on the STM sample stage. The tip was lowered into the liquid crystal droplet until a tunneling current was obtained. The excess fluid which surrounds the tip does not prevent the tunneling current to travel between the tip and graphite surface since the liquid crystal is an insulator, see Figure 14. Features portrayed in the final images, Photo 8 and Photo 9, result from the effects of the adsorbed monolayer of 6CB upon the basal plane of the graphite substrate.

A clearly resolved row-like pattern is observed in the images of 6CB. To obtain a repeat distance across the rows, a line can be drawn perpendicular to the rows. Photo 10 is like Photo 8 with a profile line included. The resulting dimensions are displayed in a profile diagram, see Figure 15. The uniform spacing between rows was determined to be 27 Å. Remaining parallel to the biphenyl segment, a single molecule of 6CB is only 14.7 Å in length. The separation distance obtained from the STM images is therefore much greater than that required for a simple alignment of single

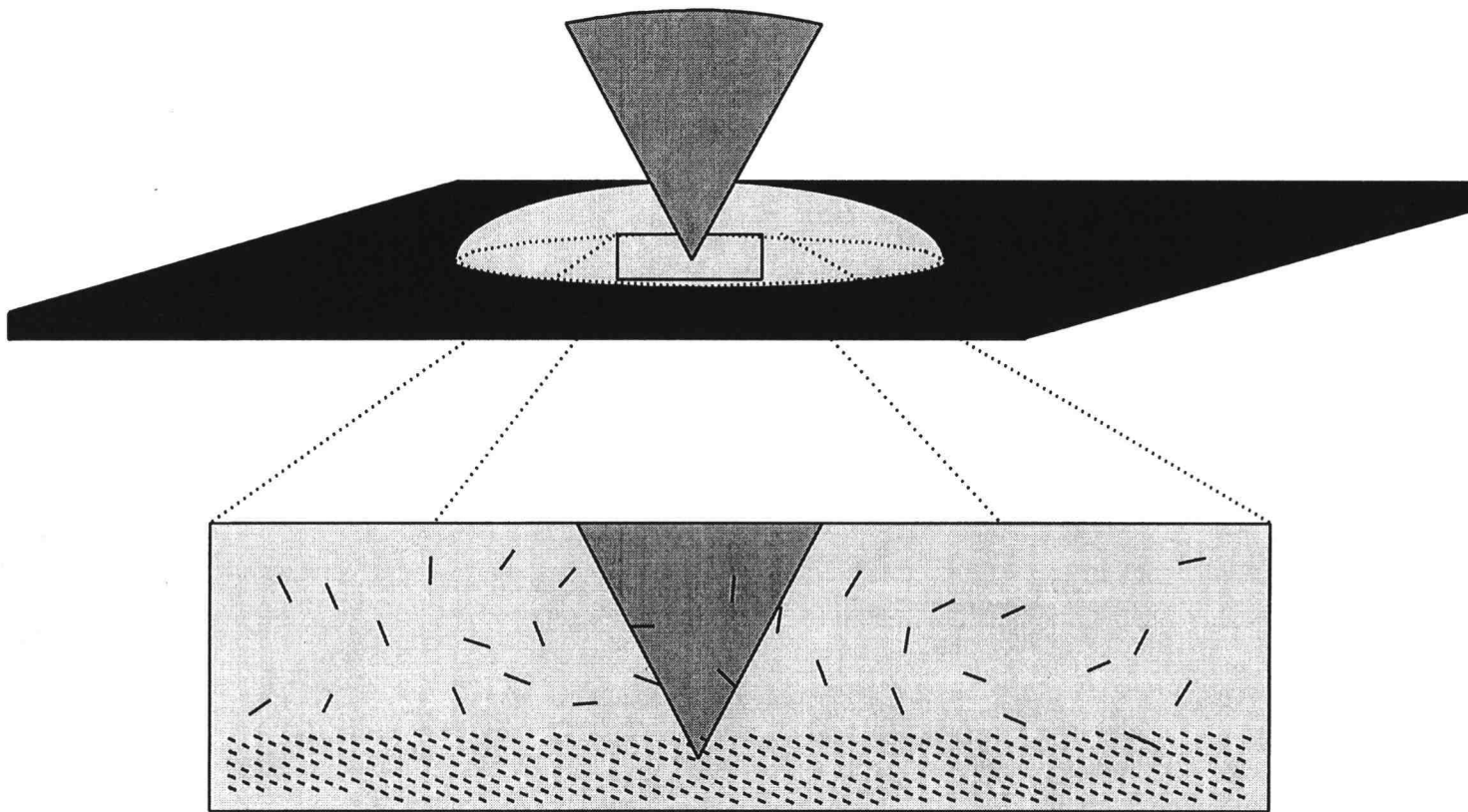


Figure 14. Illustration of STM tip pierced through the liquid droplet, able to image the surface monolayer.

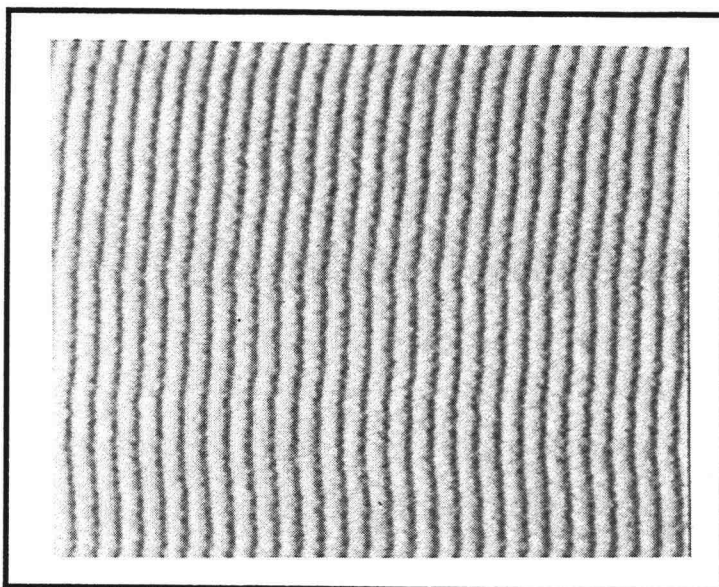


Photo 8. 6CB monolayer on graphite.  
 $750 \times 750 \text{ \AA}$ ,  $V_b = -1.0 \text{ V}$ ,  $I_t = 1.0 \text{ nA}$ .

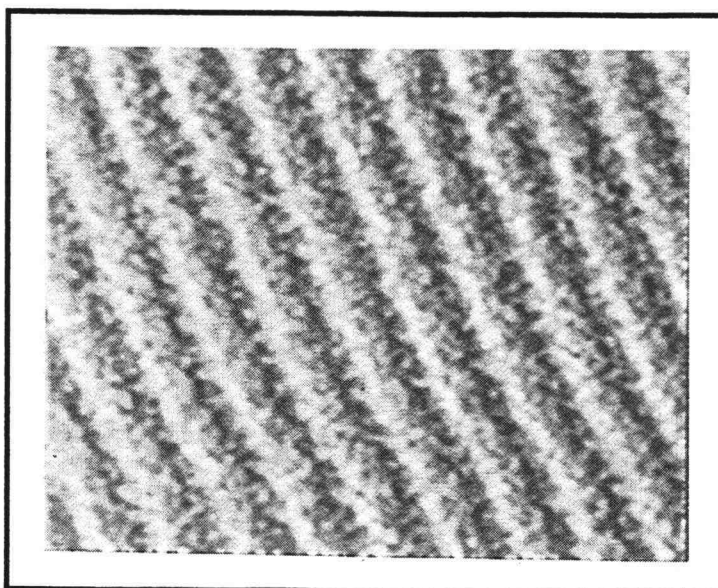


Photo 9. 6CB monolayer on graphite.  
 $225 \times 225 \text{ \AA}$ ,  $V_b = -1.35 \text{ V}$ ,  $I_t = 1.3 \text{ nA}$ .

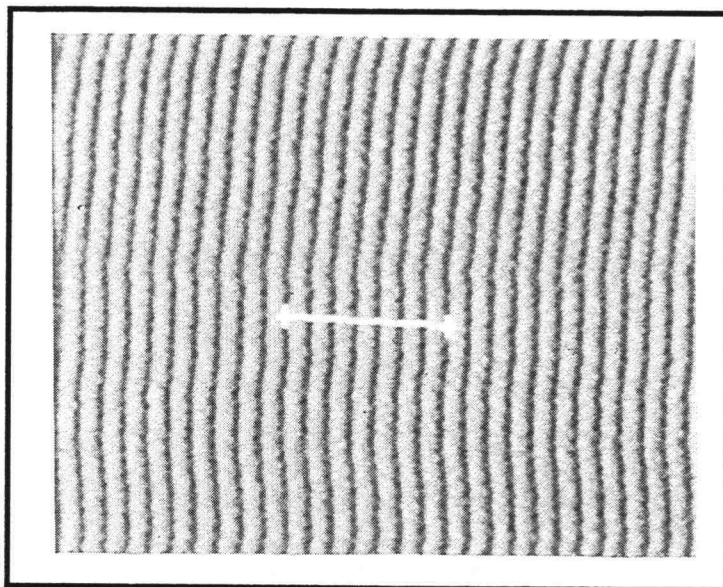


Photo 10. 6CB monolayer on graphite with profile.  
 $750 \times 750 \text{ \AA}$ ,  $V_b = -1.0 \text{ V}$ ,  $I_t = 1.0 \text{ nA}$ .

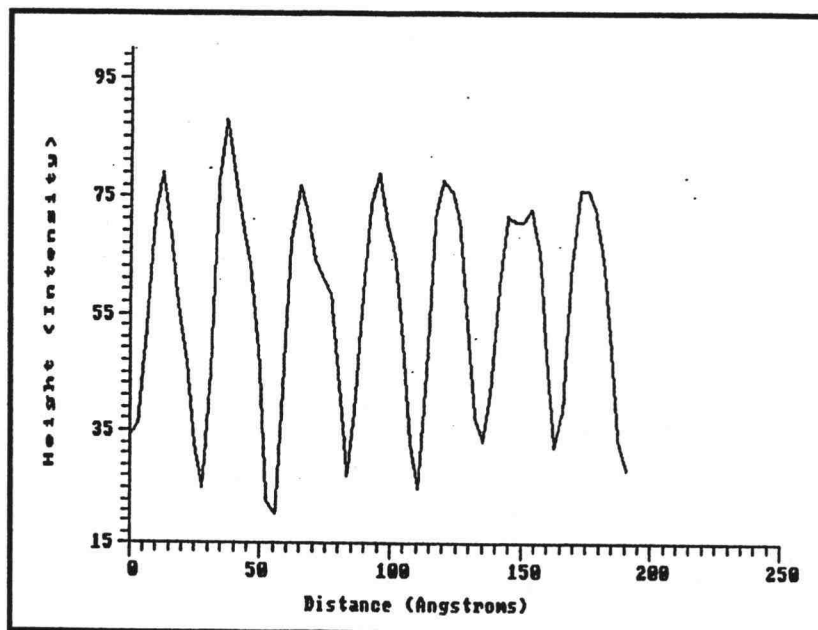


Figure 15. Profile of 6CB monolayer on graphite, refer to Photo 10.

molecular rows. It is probable that a bilayer structure with some molecular overlap would account for the resultant spacing of 27 Å.

When attempts were made to obtain better resolution, there was no success acquiring additional structural information within the rows. Individual molecules were not resolved well enough to clearly determine an exact surface structure from the 6CB images alone. For example, the separation distances between molecules perpendicular to the rows could not be resolved. More extensive results from the analysis of 8CB and 10CB, which is presented in later sections, helped to determine a possible surface structure for the 6CB monolayer. The later results suggest that the cyanobiphenyl units align head to head but offset into rows creating the brighter features while the alkyl chains are indicated by the darker valleys. It was also determined that the biphenyl head groups maintain their discrete spacing as a result of substrate lattice constraints upon surface adsorption. Since 6CB experiences greater overlap of the alkyl chains, greater separation was needed between molecules along the rows in 6CB than 8CB. Using this information and keeping reasonable interatomic distances, we can propose a reasonable structure for 6CB on graphite, see Figure 16.

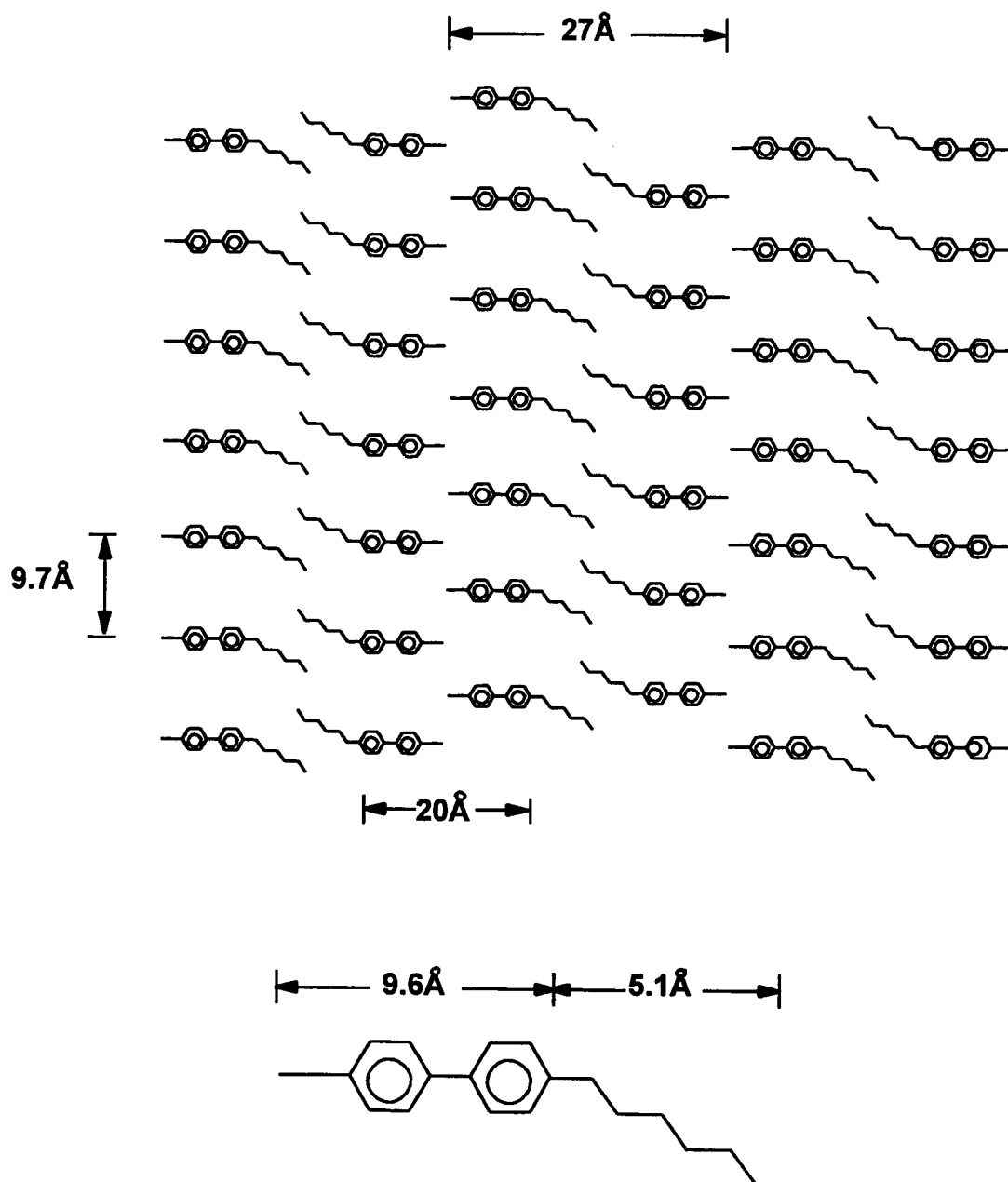


Figure 16. Proposed structure of the 6CB liquid crystal monolayer.

**OCTYL-CYANOBIPHENYL**

Typical room temperatures fall within the mesophase, 22-41°C, of the smectic liquid crystal 8CB. A white opalescent fluid, 8CB is similar to 6CB in appearance. 8CB has a greater surface tension and the sample sustained a droplet configuration upon the graphite, whereas 6CB produced a thin film. Identical sample preparation techniques were utilized as noted for 6CB. The difference in sample thickness did not appear to interfere with obtaining successful STM images.

Images of octyl-cyanobiphenyl were obtained with surface molecular features exhibiting substantial contrast. An image of a 450 x 450 Å scan, Photo 11, displays well defined rows. A profile through the image, Figure 17, provides an illustration of the 40 Å repeat distance between rows. Producing a more detailed image, a scan of a smaller surface area is portrayed in Photo 12. Detailed structure within the rows is more apparent in this photo. Unlike the 6CB results, shifts run along the rows with a periodicity which outline a subgroup structure.

Within the subgroups, eight molecules can be differentiated to define a unit cell. The brighter areas

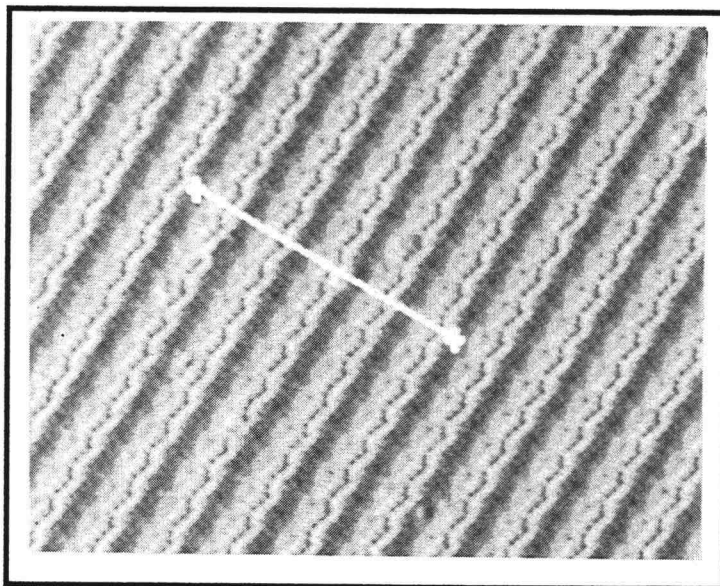


Photo 11. 8CB monolayer on graphite with profile.  
450 x 450 Å,  $V_b = 0.77$  V,  $I_t = 1.0$  nA.

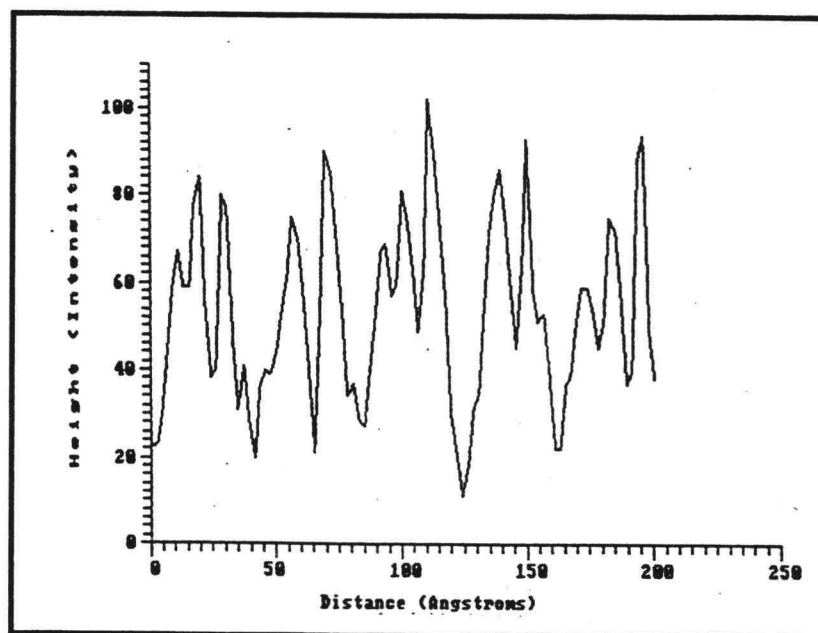


Figure 17. Profile of 8CB monolayer on graphite, refer to Photo 11.

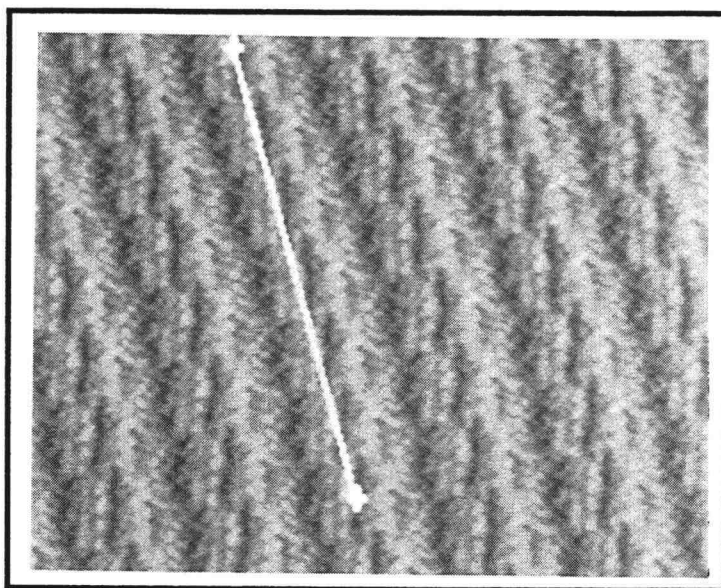


Photo 12. 8CB monolayer on graphite with profile.  
 $200 \times 200 \text{ \AA}$ ,  $V_b = -0.6 \text{ V}$ ,  $I_t = 1.0 \text{ nA}$ .

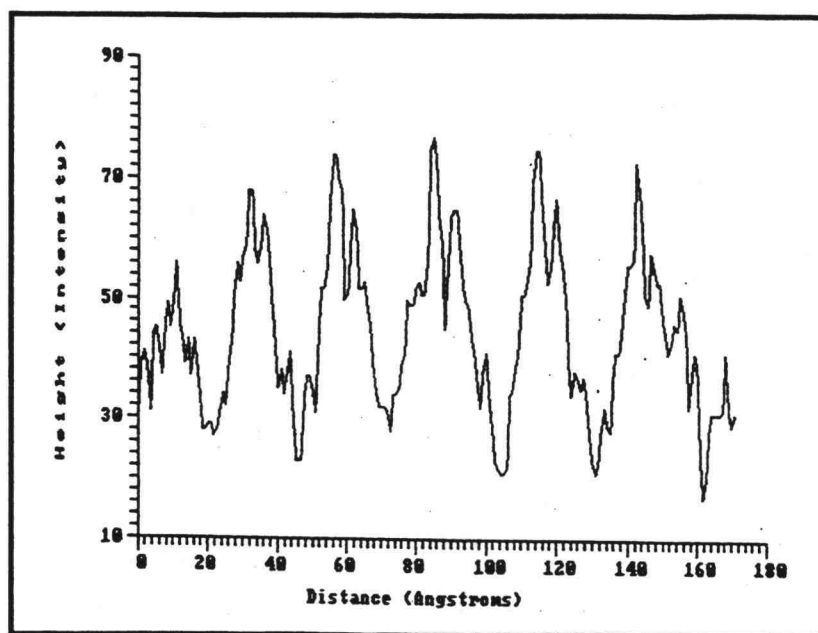


Figure 18. Profile of 8CB monolayer on graphite, refer to Photo 12.

represent the offset biphenyl groups paired head to head. The alkyl chains, or tails, lie within the darker valleys slightly overlapping. A profile aligned along a row is portrayed in Figure 18. The repeat distance which corresponds to the separation between side by side biphenyl groups is 7 Å. Between kinks along the rows, there is a 30 Å periodicity. A model of the 8CB surface monolayer on graphite is illustrated in Figure 19.

Scanning tunneling microscopy of the surface monolayer of octyl-cyanobiphenyl on graphite varies from x-ray crystallography data of the bulk material.<sup>30</sup> Table 1 summarizes results from four separate STM studies of 8CB on graphite, Smith<sup>28</sup>, Mitzutani<sup>29</sup>, Hara<sup>31</sup>, Foster<sup>26</sup> and Marty, compared to x-ray values obtained by Leadbetter<sup>30</sup>. For the bulk smectic liquid crystal, the molecules more fully interdigitate. Rows are separated by 29 Å, without kinks.

In the surface monolayer images, molecules lie 7 Å apart, indicated in column B of Table 1. This is much closer than the corresponding x-ray crystal diffraction data of 8.6 Å in the bulk state. Unable to maintain the 7 Å separation, the surface molecules must shift, producing the kink every fourth molecular bilayer along the rows. To understand how the molecules aligned so close when adsorbed

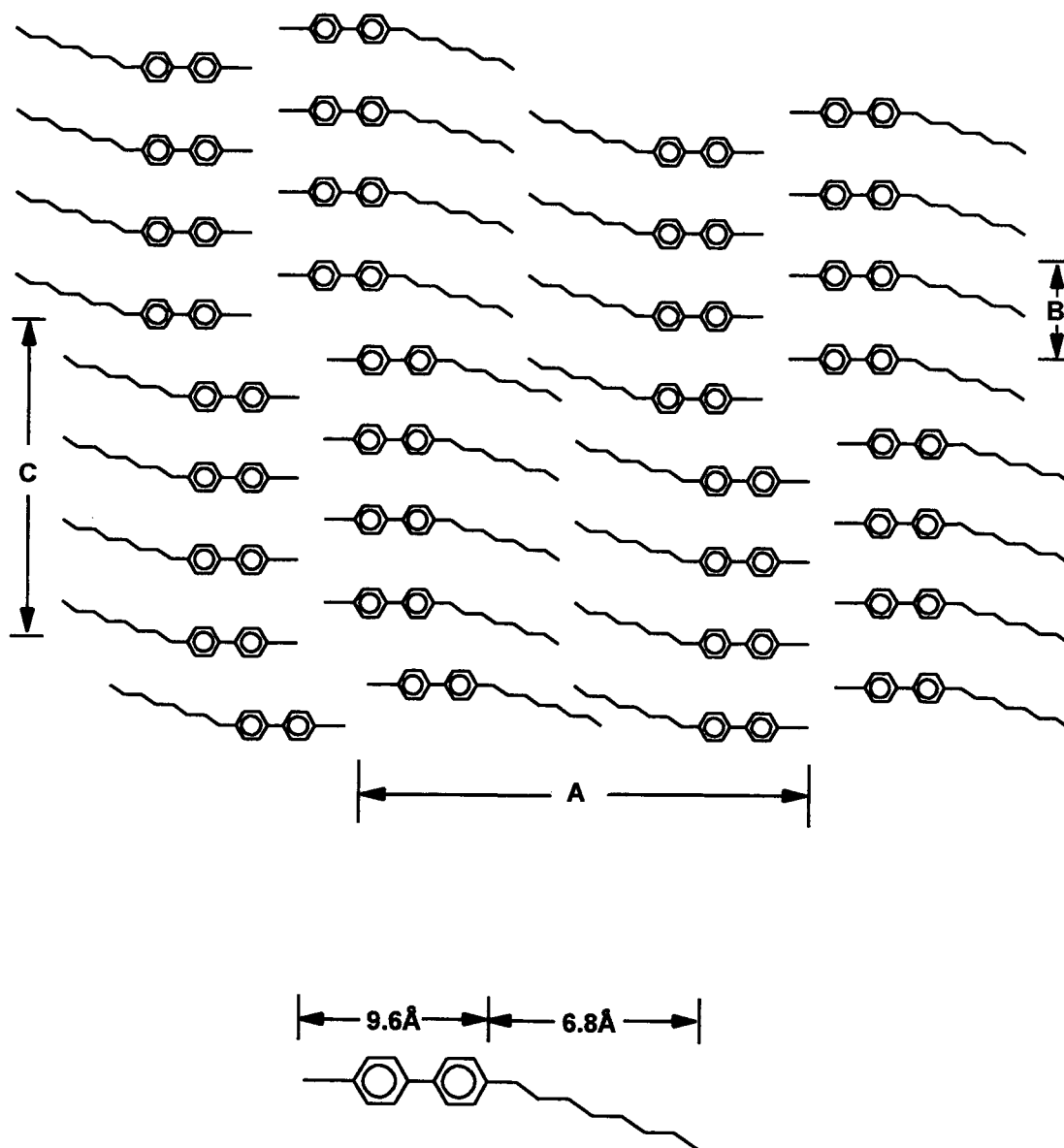


Figure 19. Proposed structure of the 8CB liquid crystal monolayer.

Others Results of STM Data for 8CB on Graphite

X-ray Crystal  
Diffraction Data

Dimension	Smith <sup>28</sup>	Mizutani <sup>29</sup>	Foster <sup>26</sup>	Hara <sup>31</sup>	Marty	Leadbetter <sup>30</sup>
A	34	38-40	34	38	40	29
B	6.5	6-7	5	7	7	8.6
C	26	n/a	n/a	n/a	28	n/a

Table 1. Values for dimensions corresponding to Figure 16.

to graphite, it is concluded that the substrate introduces constraints upon molecular orientation of the adsorbed species, and the resulting configuration is a balance of surface adsorption and intermolecular dispersion forces.

Figure 20 helps to illustrate the graphite lattice constraints upon the adsorption of both 8CB and 6CB. It is uncertain the exact geometries for the overlay, for example, whether the carbon atoms of the biphenyl groups are aligned directly above the carbon atoms of the substrate or if they alternate like the ABA stacking pattern of graphite. In either case, the figure helps to illustrate the dimensional relationships observed for 8CB, and why 9.6 Å was determined to be the separation distance between 6CB molecules in Figure 16. A distance of 7.2 Å was not chosen since there were no kinks within the rows of 6CB monolayers on graphite and the next equivalent adsorption site provided the 9.6 Å value.

Using TiO<sub>2</sub> as a substrate, another image of an octyl-cyanobiphenyl monolayer is shown in Photo 13. A film is apparent when compared to the clean TiO<sub>2</sub> image illustrated in chapter three. There are no unit cells or other structural features which can be detected, nor was the resolution of the STM able to see individual 8CB molecules.

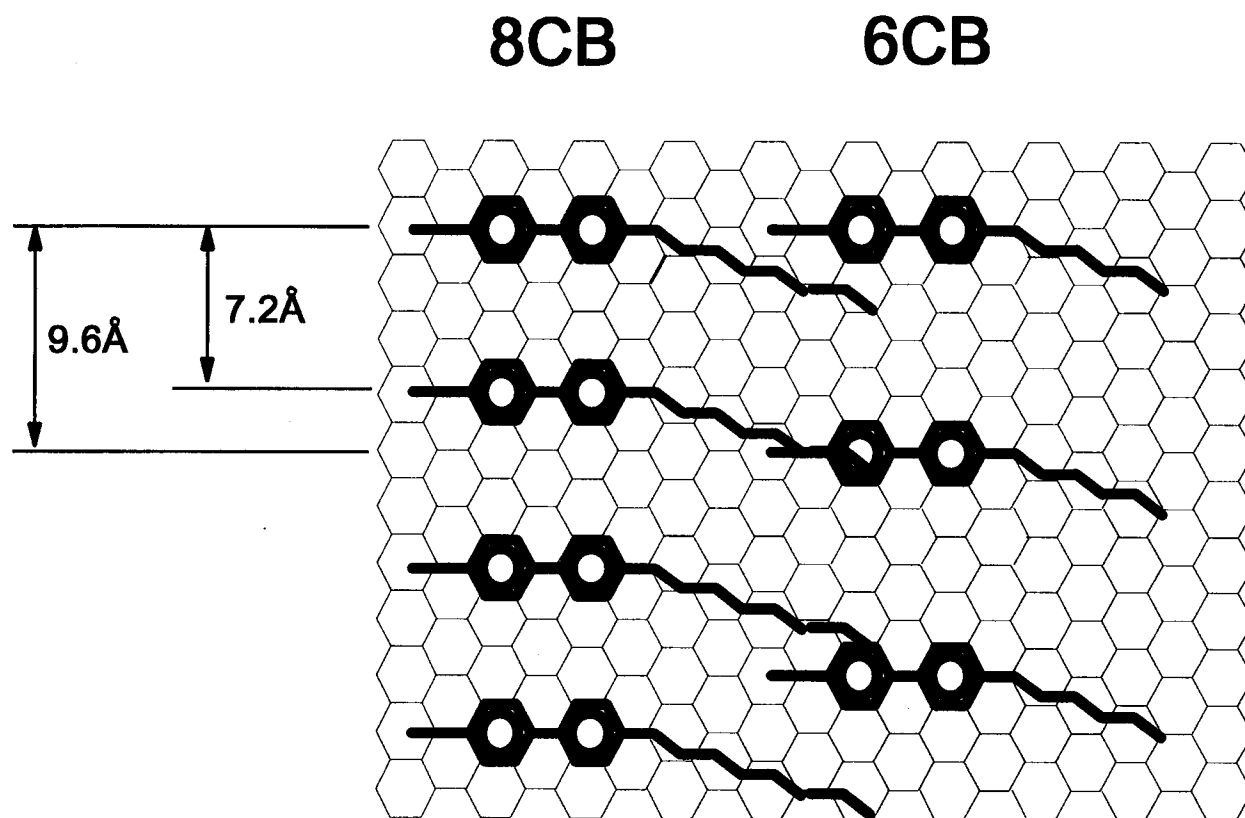


Figure 20. Overlay of 8CB and 6CB molecules on graphite.

Such a rough surface could not sustain long range surface molecular ordering needed for a truly successful STM image.

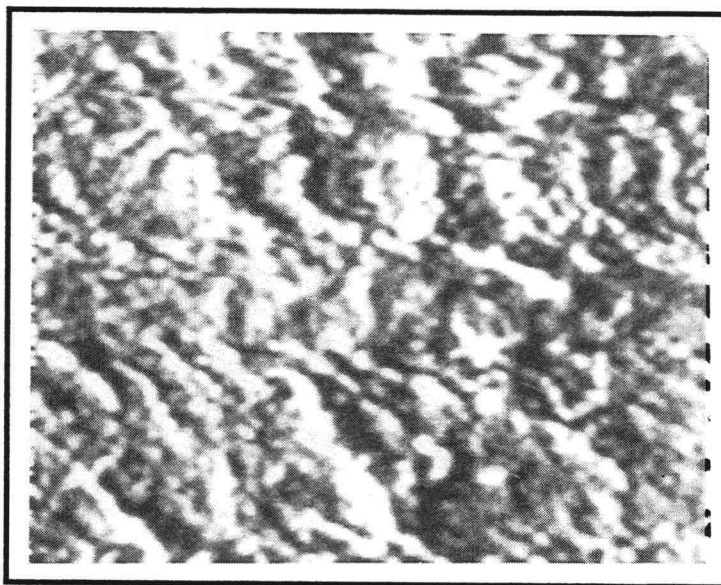


Photo 13. 8CB on titanium oxide surface.  
 $0.16 \times 0.17 \text{ } \mu\text{m}$ ,  $V_b = -3.5 \text{ V}$ ,  $I_t = 0.75 \text{ nA}$ .

#### **DECYL-CYANOBIPHENYL WITH SOLVENT STUDY RESULTS**

For 10CB, the mesophase is  $44\text{-}51^\circ\text{C}$ , well above typical room temperature conditions. In order to image 10CB, two sample preparation techniques were utilized in this study. The first technique was to maintain a heated sample just above  $44^\circ\text{C}$ , producing a neat surface monolayer. The second method involved the dissolution of the liquid crystal in a solvent. Decane and dodecane were employed separately as solvents in this study.

To prepare a neat sample, a small amount of the colorless opaque 10CB crystalline material was placed on a freshly cleaved surface of graphite. The sample and substrate were then placed on a hot plate until the sample melted. The heated 10CB covered graphite was then transferred to the preheated sample stage. By coiling heating tape around the aluminum microscope cover, the microscope stage as well as the scanning head were heated. A variac is used to regulate the microscopes temperature. Only to save time was the sample-substrate transferred from a hot plate to the warmed stage. Before obtaining an image the power to the variac was turned off to eliminate possible interference from the electromagnetic currents carried throughout the heating element. To avoid thermal drift, the cover remains on while scanning the surface. The temperature remains consistent long enough to obtain several scans, before the sample crystallized. An image of the neat 10CB monolayer is given in Photo 14.

When preparing the liquid crystal solution, either decane or dodecane was used as the solvent. The initial concentration of the solution was made approximately 0.25 M. A thin film results from a drop of the solution placed on the graphite substrate. The solvent evaporates, leaving crystalline 10CB upon the surface. In order to keep the

graphite covered with the 10CB solvent mixture, a small cup was designed to hold a sufficient volume of the sample solution, see Figure 21. The choice of solvents was selected based on their acceptably low evaporation rate. While the solvent in the cup evaporates slowly, the effective concentration of 10CB would increase. This factor did not appear to affect the image, as long as there was enough solvent to keep the liquid crystalline material in solution. Photos 15 and 16 are images of 10CB in decane and dodecane respectively.

There are some strong similarities between these three images of 10CB on graphite. Like the features displayed by 8CB on graphite, there are distinct rows observable. The subgroup structure within the rows is most clearly evident in the images obtained by solvent preparation. Unlike 8CB, the 10CB monolayer has ten molecules which make up the subgroup. The neat monolayer results provide a less pronounced image. The kinks are still present within the rows, though it is difficult to resolve the molecules. Results by Smith et. al.<sup>28</sup>, of heated 10CB on graphite provided greater resolution than presented in Photo 14. This indicates that thermal motion created the more blurry image and that the system was not sufficiently insulated. A generalized model of the proposed structure is presented in

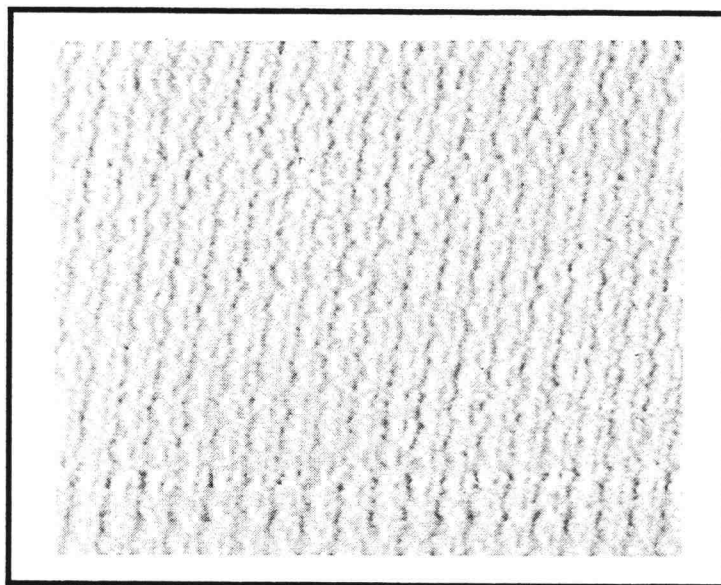


Photo 14. Neat 10CB on graphite.  
 $750 \times 750 \text{ \AA}$ ,  $V_b = 1.5 \text{ V}$ ,  $I_t = 0.88 \text{ nA}$ .

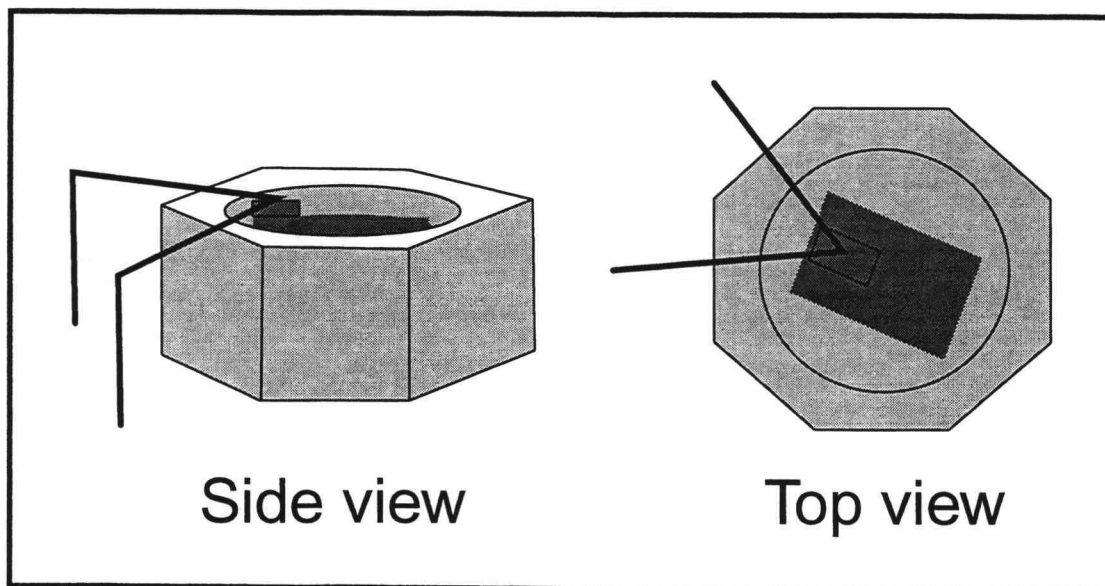


Figure 21. Illustration of machined aluminum cups used to maintain graphite substrate immersed in 10CB sample-solvent solution.

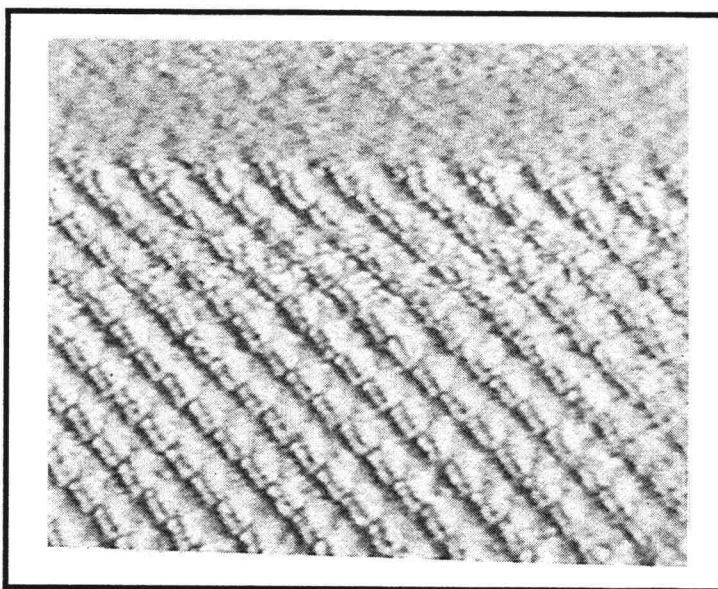


Photo 15. 10CB on graphite from a decane solution.  
 $550 \times 500 \text{ \AA}$ ,  $V_b = -2.0 \text{ mV}$ ,  $I_t = 1.0 \text{ nA}$ .

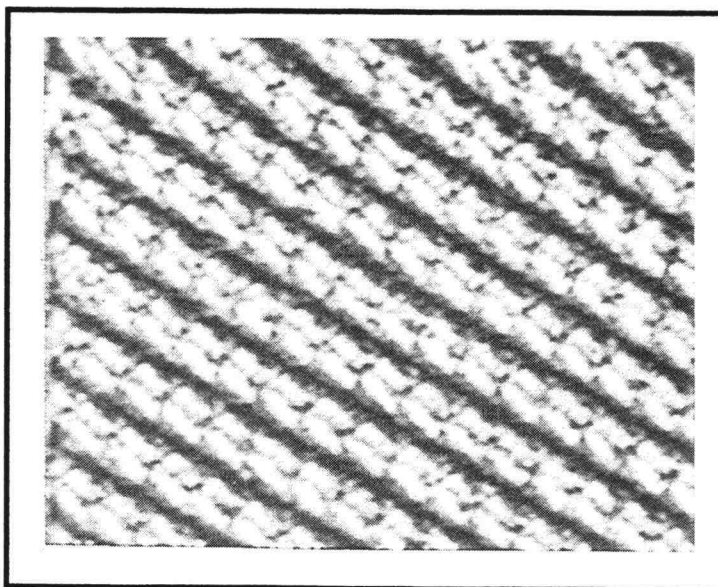


Photo 16. 10CB on graphite from a dodecane solution.  
 $410 \times 400 \text{ \AA}$ ,  $V_b = -1.0 \text{ mV}$ ,  $I_t = 0.9 \text{ nA}$ .

Figure 22, with the exact dimensional values from each system summarized in Table 2.

Comparing dimensions of the surface molecular features, all of the corresponding values in Table 2 agree well within experimental error except for the variation in separation distance between rows. Examining the images closely, the distance along the biphenyl group remains consistent. It is the length between the biphenyl groups, where the alkyl chains lie, that the increased separation distance is accounted for when the dodecane is present. The images do not present great detailed features in the valleys. The greater contrast which helps to calculate dimensions is found within the biphenyl head groups.

To increase the intermolecular separation, it appears that the dodecane interacted with the liquid crystal monolayer enough to alter the surface adsorption sites. In solution, the alkane solvent molecules have a greater affiliation with the alkyl group of the liquid crystal than the biphenyl group. It is proposed that the solvent molecules maintain an interaction with the liquid crystal until surface adsorption occurs. The dodecane solvent, being longer than the alkyl chain of 10CB, places a demand for greater separation between rows. Decane, on the other

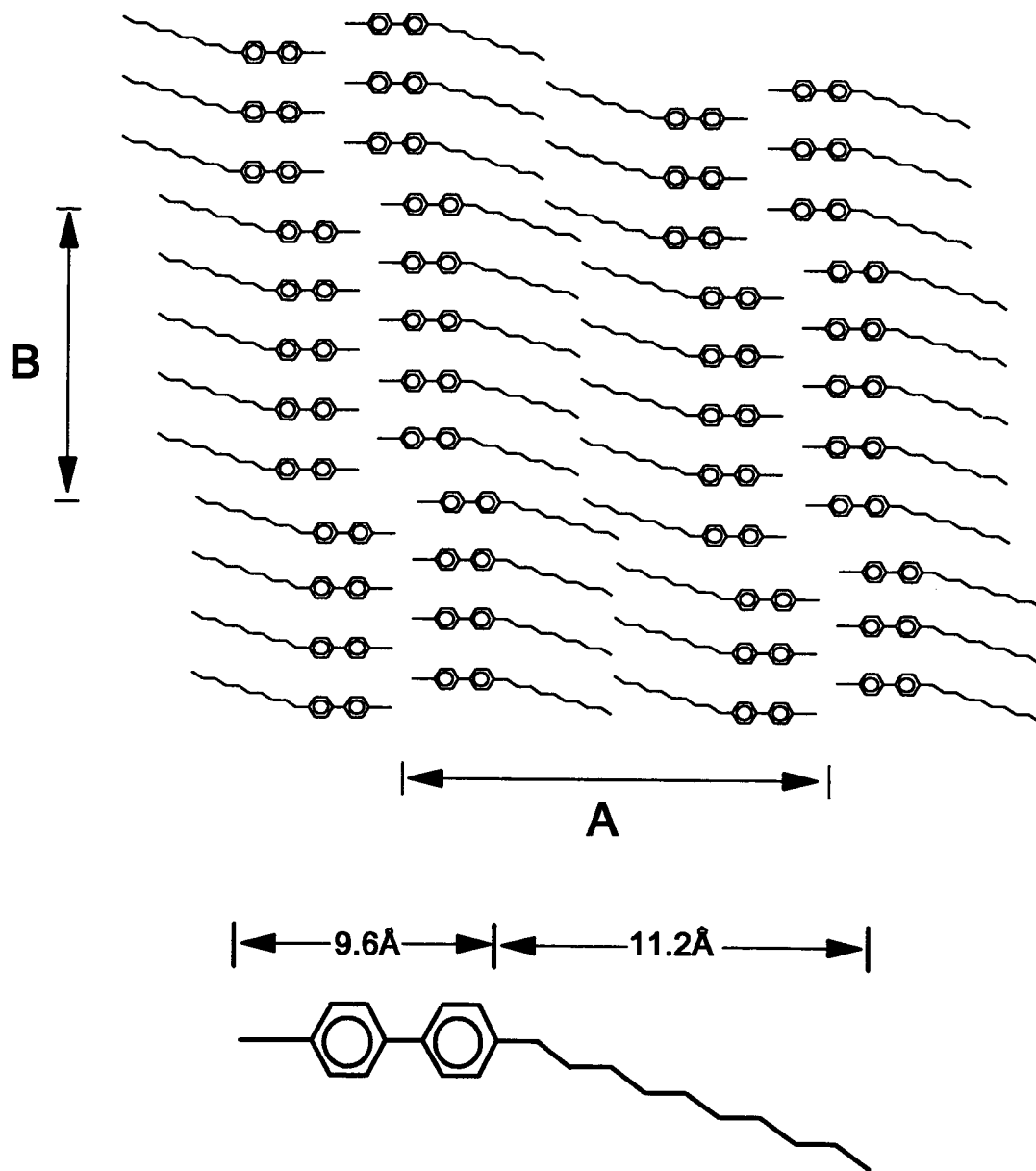


Figure 22. Proposed monolayer structure for 10 CB adsorbed on graphite. See Table 2 for the appropriate dimensions.

Dimension	Neat	Decane	Dodecane
A	43	42	50
B	32	33	33

Table 2. Values for dimensions corresponding to Figure 22.

hand, would be similar in length to the alkyl chain and would not create any additional strain. It follows that the decane solvent results agree well to those of the heated 10CB results.

To justify the increased separation between rows of 10CB molecules, the added length of the dodecane rather than the decane solvent would be much less than the 8 Å variation observed. Graphite lattice constraints produce a more likely answer, see Figure 22. For the biphenyl groups of the liquid crystal to maintain an equivalent adsorption environment, the molecules would need to shift horizontally across the graphite lattice spacing of 8.4 Å.

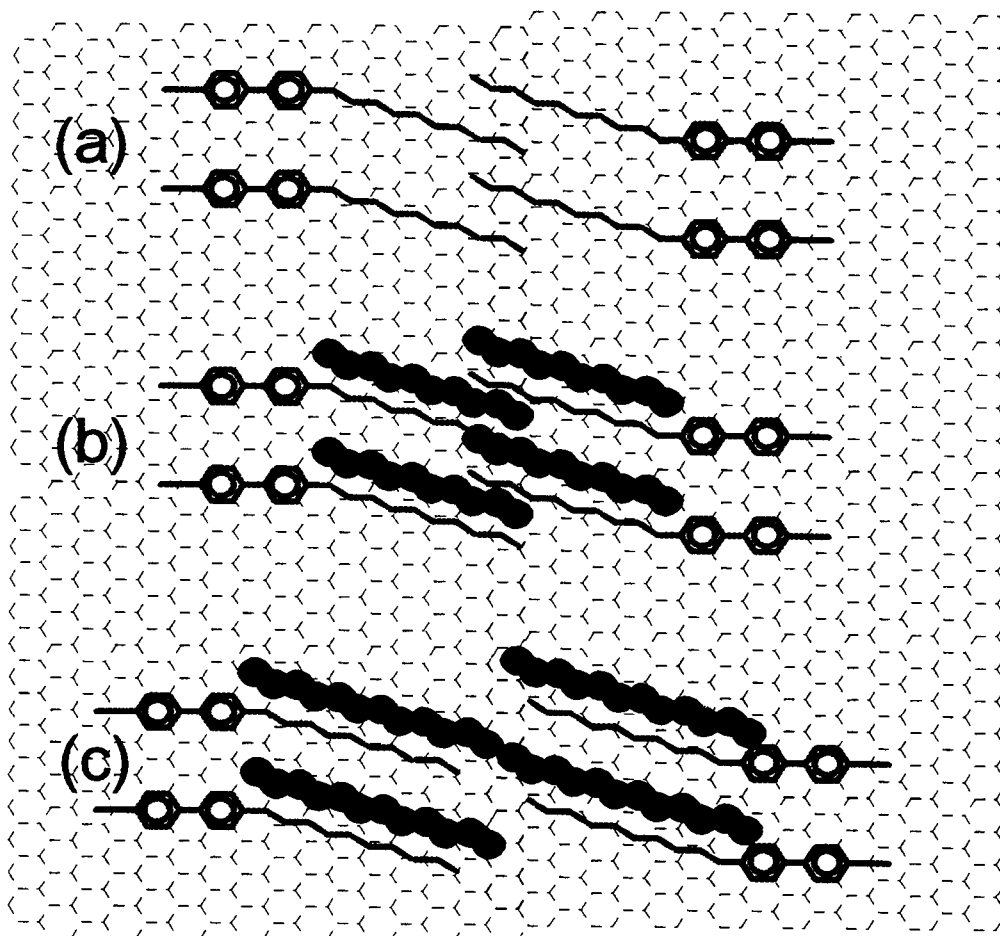


Figure 23. Overlay of 10CB molecules on graphite.

(a) Neat sample, no solvent. (b) Decane molecules interact with alkyl chain, does not affect surface adsorption sites. (c) Dodecane molecules force the liquid crystal molecules apart.

**ALKANES AND CARBOXYLIC ACIDS**

The first STM images of solid dotriacontane,  $n\text{-C}_{32}\text{H}_{66}$ , from a decane solution were reported by McGonigal et al.<sup>32</sup> They were consistent with microcalorimetry studies of Groszek<sup>33</sup> which showed that  $n\text{-C}_{32}\text{H}_{66}$  is preferentially adsorbed onto the graphite surface from solutions of lighter hydrocarbon molecules. Groszek's work illustrated that the adsorption was extremely independent of concentration and also suggested the formation of a stable monolayer of dotriacontane molecules remaining parallel to the surface.

STM images of dotriacontane are presented in both Photo 17 and Photo 18. The sample was prepared by dissolving a small amount of the solid  $n\text{-C}_{32}\text{H}_{66}$  into decane, then placed on a piece of HOPG in an aluminum cup as illustrated in the previous section. These results agreed well with those from McGonigal's experiments. The length of one molecule is approximately 40 Å. The width of the rows were observed to be 48Å, which allows for a reasonable distance between the rows of molecules. Spacing between molecules perpendicular to the rows are at 4.5 Å.

The presence of a carboxylic acid functional group also provided relatively successful images. Photo 19,

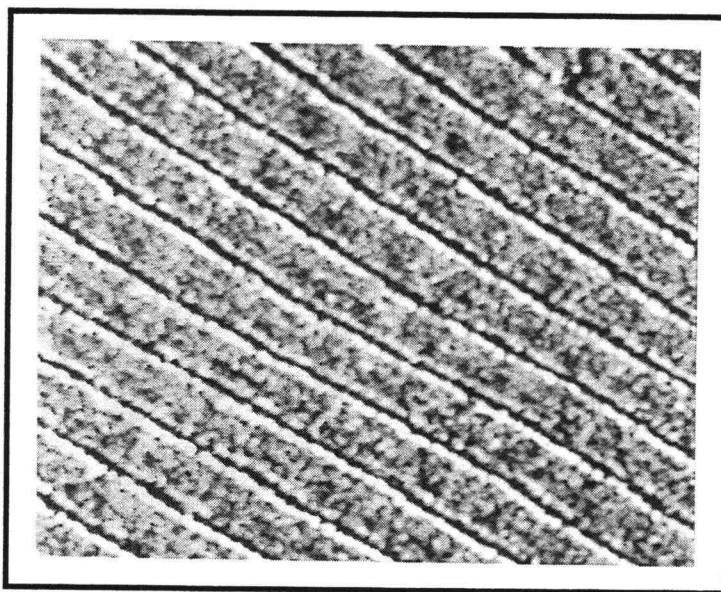


Photo 17.  $C_{32}H_{66}$  on graphite from a decane solution.  
 $450 \times 450 \text{ \AA}$ ,  $V_b = 1.0 \text{ V}$ ,  $I_t = 1.5 \text{ nA}$ .

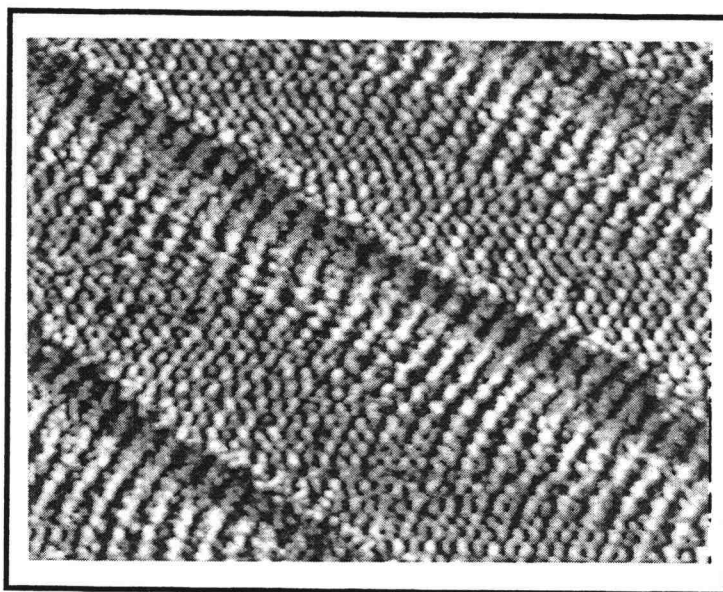


Photo 18.  $C_{32}H_{66}$  on graphite from a dodecane solution.  
 $110 \times 110 \text{ \AA}$ ,  $V_b = 0.6 \text{ mV}$ ,  $I_t = 0.8 \text{ nA}$ .

illustrates an image of a tricontanoic acid monolayer on graphite prepared from a decane solution. The detection of rows indicates molecular alignment, although the clarity obtained was consistently less than that of the simple alkane chain. This effect could be due to the system featuring weaker surface adsorption resulting in more thermal motion of the monolayer. The dimension between rows, Photo 19, is similar to that of dotriacontane at 40 Å, although the intermolecular spacing could not be resolved.

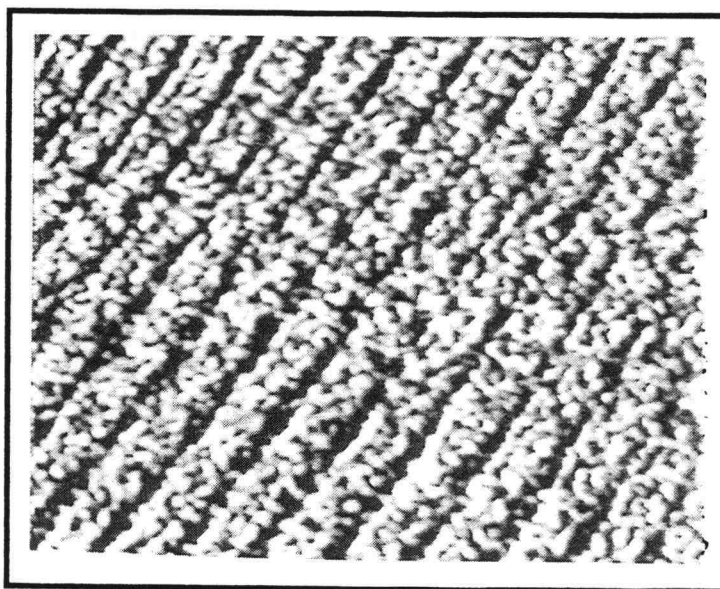


Photo 19. Tricontanoic acid on graphite from a decane solution.  
450 x 450 Å,  $V_b = 0.4$  V,  $I_t = 2.0$  nA.

## SUMMARY

For STM analysis of organic fluids, the choice of a substrate is critical to the success of the images. The substrate must meet three criteria, the ability to sustain a tunneling current, retain an atomically flat surface over the area scanned, and immobilize a monolayer of the sample. Substrates and preparation techniques mentioned in this study include graphite prepared by surface cleavage, gold deposited on mica by vacuum evaporation, and titanium oxide prepared by mechanical and chemical polishing.

The adsorption geometries created by the liquid crystalline series provided magnificent detailed features of the sample monolayer on graphite. The quality or amount of information available from any image is dependent upon the existence of molecular symmetry within the monolayer on the substrate surface. Observed long range features provide valuable information about the system. If samples were to adsorb randomly, the resultant image would be blurred, and the only information possible would be that of resolved individual molecules.

In this study, sample and substrate preparation techniques used for creating STM images are factors which

affect sample interpretation. As found with the 10CB solvent study , the sample preparation methods and the substrate lattice constraints greatly affect the results of an STM image. These are fundamentally important factors when interpreting STM data, and need consideration when analyzing results. The information provided by a successful STM image does not need to be only what is 'seen', or the dimensions of the features. Interpretations of resolved features are required to provide the more fundamental as well as the more difficult results that are desired from a scanning tunneling microscope. Those that provide additional understanding of localized sample-substrate adsorption mechanisms, and are possibly capable of answering how the observed image is produced.

## REFERENCES

- 1 *The American Heritage Dictionary of the English Language. New College Edition* (1979).
- 2 E. Ruska *Angew. Chem. Intl. Ed.* **26**, 567 (1987).
- 3 E. Slayter and H. Slayter. *Light and Electron Microscopy*, Cambridge University Press, (1992).
- 4 G. Binnig and H. Rohrer, *Sci. Am.* **253**, 50 (1985).
- 5 B. Binnig, H. Rohrer, C. Gerber and E. Weibel, *Sur. Sci.* **131**, L379 (1983).
- 6 G. Binnig and H. Rohrer, *Angew. Chem. Int. Ed. Engl.* **26**, 606 (1987).
- 7 G. Binnig, H. Rohrer, C. Gerber and E. Weibel, *Phys. Rev. Lett.* **50**, 120 (1983).
- 8 R. Becker and R. Wolkow, p.149 in *Scanning Tunneling Microscopy*, (J. Stroscio and W. Kaiser, eds.), Academic Press, (1993).
- 9 G. Binnig, H. Rohrer, C. Gerber and E. Weibel, *Surf. Sci.* **131**, L379 (1983).
- 10 S. Park and R. Barrett, p.33 in *Scanning Tunneling Microscopy*, (J. Stroscio and W. Kaiser, eds.), Academic Press, (1993).
- 11 J. Tersoff and N.D. Lang, p.1 in *Scanning Tunneling Microscopy*, (J. Stroscio and W. Kaiser, eds.), Academic Press, (1993).
- 12 J. Bardeen, *Phys. Rev. Lett.* **6**, 57 (1961).
- 13 G. Binnig, H. Rohrer, C. Gerber and E. Weibel, *Phys. Rev. Lett.* **49**, 57 (1982).

- 14 P. Hansma and J. Tersoff, *J. Appl. Phys.* **61**, R1 (1987).
- 15 P. Avoris, *J. Phys. Chem.* **94**, 2246 (1990).
- 16 W. Sacks and C. Noguera, *Phys. Rev. B* **43**, 11612 (1991).
- 17 N. Barniol, E. Farres, F. Martin, J. Sune, I Placencia and X. Aymerich, *Vacuum* **41**, 379 (1990).
- 18 J. Tersoff and D. Hamann, *Phys. Rev. B* **31**, 805 (1985).
- 19 S. Chang, p.182 in *Scanning Tunneling Microscopy I*, (H. Guntherodt and R. Wiesendanger, eds.), Springer-Verlag, (1992).
- 20 W. Reynolds, *Physical Properties of Graphite*, Elsevier, (1968).
- 21 C. Clemmer and T. Beebe, *Science* **251**, 640 (1991).
- 22 F. Fan and A. Bard, *J. Chem. Phys.* **94**, 3761 (1990).
- 23 R. Emch, J. Nogami, M. Dovek, C. Lang and C. Quate, *J. Appl. Phys.* **65**, 79 (1989).
- 24 C. Widrig, C. Alves and M. Porter, *J. Am. Chem. Soc.* **113**, 2805 (1991).
- 25 E. Holland-Moritz, J. Gordon, G. Borges and R. Sonnenfeld, *Langmuir* **7**, 301 (1991).
- 26 J. Foster and J. Frommer, *Nature* **333**, 542 (1988).
- 27 J. Spong, H. Mizes, L. LaComb, M. Dovek, J. Frommer and J. Foster, *Nature* **338**, 137 (1989).
- 28 D. Smith, J. Horber, G. Binnig and H. Nejh, *Nature* **344**, 641 (1990).
- 29 W. Mizutani, M. Shigeno, M. Ono and K. Kajimura, *Appl. Phys. Lett.* **56**, 1974 (1990).

- 30 A. Leadbetter, J. Frost, J. Gaughan, G. Gray and A. Mosley, *J. Phys., Paris* **40**, 375 (1979).
- 31 M. Hara, Y. Iwakabe, K. Tochigi, H. Sasabe, A.F.Garito and A. Yamada, *Nature* **344**, 228 (1990).
- 32 G. McGonigal, R. Bernhardt and D. Thomson, *Appl. Phys. Lett.* **57**, 28 (1990).
- 33 A. Groszek, *Proc. Roy. Soc. London Ser. A* **314**, 473 (1970).